Jet Quenching in the Compact Muon Solenoid at the LHC

by

David López Mateos

Submitted to the Department of Physics
in partial fulfillment of the requirements for the degree of

Bachelor of Science in Physics

at the

MASSACHUSETTS INSTITUTE OF TECHNOLOGY

June 2005

Author .....
Department of Physics
June, 2005

Certified by .....
Bolesław Wysłouch
Professor, Department of Physics
Thesis Supervisor

Accepted by .....
David E. Pritchard
Senior Thesis Coordinator, Department of Physics

Jet Quenching in the Compact Muon Solenoid at the LHC

by

David López Mateos

Submitted to the Department of Physics
on June, 2005, in partial fulfillment of the
requirements for the degree of
Bachelor of Science in Physics

Abstract

In this thesis we perform analyses on simulated data that allow us to demonstrate the sensitivity of the CMS experiment to certain jet quenching observables. In particular, two theoretical scenarios which mimic RHIC data at low p_T and which show either no quenching or BDMPS-based quenching at high p_T are formulated. The difference between these two scenarios is analyzed for R_{AA}, R_{CP} at different centralities and jet-specific observables such as jet energy spectra, fragmentation functions and jet profiles. We show how these analyses indicate that the large acceptance of the CMS detector, combined with the high granularity in the energy resolution of the calorimeter will be essential tools in studying the phenomenon of jet quenching. Finally, we propose extensions to this work in preparation to analyzing the data from *Pb-Pb* runs at the LHC.

Disclaimer: The work on this thesis does not model the CMS detector geometry with the accuracy required for official analyses, which are fully representative of the CMS detector capabilities. Such analyses require of the full CMS simulation machinery and are left to the CMS Heavy Ion group as a whole.

Thesis Supervisor: Bolesław Wysłouch
Title: Professor, Department of Physics

Acknowledgments

I would like to warmly acknowledge all the CMS and MIT Heavy-Ion Groups without whose members this thesis would not have been possible. I want to very specially thank Bolek Wyslouch and Christof Roland whose exceptionally dedicated supervision has made this research project an unforgettable learning and personal experience. I also acknowledge the help received from Igor Lokhtin and Alexandre Sniguirev in all the issues related to the Monte Carlo generators and theoretical models. I want to also thank Gunther Roland for providing initial supervision and help with different Physics questions all throughout the duration of the project. Also great thanks to Maarten Ballintijn for helping with the development of CMSROOT, logistics issues and reviewing the drafts of the appendix. Finally, I would like to very specially thank my family, relatives and close friends, and in particular, my father, Ricardo López Fernández whose unconditional support has allowed me to complete this and all other challenges I have faced.

The list of people from whom I have received support through my undergraduate years is long and cannot be written in full here. However, to all those who showed such support: Thank you very much.

Contents

Chapter 1

Introduction

Quarks are the smallest subdivision of matter as we know it today. Quarks group to form different elementary particles, protons and neutrons among them. All matter is made of atoms whose nuclei are composed by these elementary particles. The theory that explains the interactions between quarks is known as Quantum Chromodynamics (QCD). Like in the Quantum Theory of Electromagnetism (QED), where the interactions happen through photon exchange; there is a carrier of force in QCD which is called the gluon. While the QCD and QED Lagrangians have a similar structure, the larger set of symmetries inherent to QCD lead to a much more complex phenomenology. In particular, the SU(3) color charge symmetry of QCD and its non-Abelian property imply that gluons carry color charges (unlike in QED, where the photon has no charge). This in turn leads to a scale-dependent or running coupling constant which is unprecedented in QED and which, to leading order, can be written as proposed by F. Wilczek and D. Gross in [1]:

$$\alpha_s(Q^2) = \frac{4\pi}{\left(11 - \frac{2}{3}n_f\right)\log Q^2/\Lambda^2_{QCD}}; \tag{1.1}$$

where Q^2 is the energy scale, n_f the number of active flavors (i.e.: number of quarks with energy less than the energy scale) and Λ^2_{QCD} is defined as the scale at which the coupling becomes large (when $Q^2 \sim \Lambda^2_{QCD}$). A similar relation has been found for the effective coupling constant as a function of temperature $\alpha_s(T)$ [2].

This running coupling constant signals the existence of one of the characteristic features of QCD; namely *confinement*. Confinement is the property which describes the empirical fact that isolated color charges have never been found, and that all known particles have a neutral color charge. This empirical fact has an explanation in the context of the Equation 1.1 through the divergence of α_s at low energies or large distances, which makes it impossible to separate two color charges without putting an infinite amount of energy into the system. This picture gives qualitative insight into the mechanism of confinement within QCD.

1.1 The Quark-Gluon Plasma

A concept which is closely related to that of confinement is that of *asymptotic freedom*. This concept also describes an experimental observation, namely the one made by J. I. Friedman, H. Kendall and R. E. Taylor [5] in which they saw that confined quarks interact weakly among them. This observation is also reflected on Equation 1.1 at high energies or short distances. Considering this weakening of the Strong Interactions at high temperatures or densities, we could intuitively argue that under such conditions we have a new quark matter in which short-range interactions with neighboring quarks are weak, long-range interactions are screened and, therefore, quarks are in fact deconfined. This hypothesis has been in fact corroborated by calculations of lattice QCD [3] (Figure 1-1).

This new state of matter, called the Quark-Gluon Plasma (QGP), is characterized by an energy density of [3]

$$\epsilon \equiv \epsilon_{q+\bar{q}} + \epsilon_g = \left(6n_f \frac{7\pi^2}{120} + 16\frac{\pi^2}{30}\right) T^4. \tag{1.2}$$

The experimental study of the properties of this new state of matter requires the generation of extreme conditions of high energy density and temperature (note that 170 $MeV \sim 10^{12}$ K). Such conditions can only be achieved in the laboratory

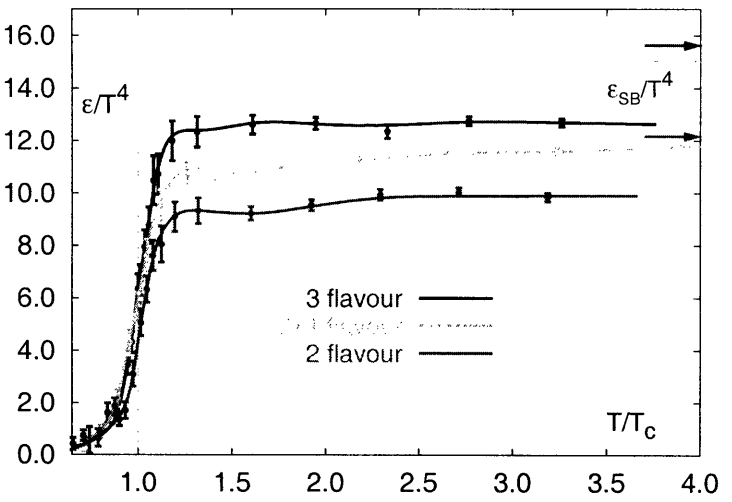

Figure 1-1: Energy density as a function of temperature from lattice QCD [3]. The critical temperature at which the phase transition occurs T_c is around 170 MeV for 2 active flavors and 150 MeV for 3 active flavors. The arrows show the value of ϵ arising from Equation 1.2. We can see that the ideal values for a truly free gas of quarks are not reached due to remaining strong interactions in the QGP. Nevertheless, the phase transition is clearly present.

today in ultrarelativistic heavy-ion collisions at different colliders around the world. Much has been learnt from the Relativistic Heavy-Ion Collider (RHIC), currently the world's highest energy accelerator of heavy ions. Some of these findings will be discussed in Chapter 2, and more extensive reviews can be found elsewhere [4, 40]. However, there are still many open questions regarding the properties of the QGP and the interactions inside it. Many of these questions require the study of the QGP in a new energy regime which will only become available for experimental studies at the next-generation heavy-ion collider, the Large Hadron Collider (LHC). This new energy regime will not only allow us to create a QGP which is longer-lived and has a higher energy density, but will also provide us with new tools to study the interactions inside this medium. One of the most promising such tools is what is known as jet quenching[4, 6, 7].

1.2 Hard Probes: Jet Physics

Before giving the definition of a jet, let us go back to Equation 1.1. Notice that for large-momentum-transfer processes, α_S becomes small, and analytic calculations through perturbation theory become possible. In this context, we can understand why these so-called *hard processes* played such an important role in the first tests of QCD. In particular, the experimental study of these hard processes was performed through the study of the properties of the final state particles produced in the collisions of simple QCD systems such as e^+e^-, two protons or a proton and an antiproton[1] [8]. In the spirit of confinement and the running coupling constant, we can understand some qualitative features of these final state particles as follows. When a large-momentum-transfer scattering occurs in a high-energy collision in such a simple system, as the original scattered partons separate, the energy in the strong field between them becomes bigger and bigger until there is enough energy to create a new quark-antiquark pair [10]. This process results in the production of two sets of particles travelling in opposite directions and concentrated in two small cones around the direction of the two original partons after the scattering process. These sets of particles were called *QCD jets*.

Summarizing, a **QCD jet** is the highly collimated set of hadronic particles generated by a high-momentum-transfer scattering due to strong interactions at the partonic level. While this definition is simple and gives insight into the nature of a jet, it is experimentally rather simplistic and not suitable as we will discuss in Chapter 3. An illustration of the generation of such a QCD jet is shown in Figure 1-2.

In principle, extrapolating the description of a hard process given above and in the absence of a phase transition and the resulting collective phenomena, we would expect many such jets to appear in more complex systems such as those encountered in heavy-ion collisions. The absence of such a superposition in fact has been pointed as one of the signatures of the existence of the QGP[12]. However, even if the QGP is formed over the region of space where the heavy-ion collision occurs, we do expect to

[1]We refer to these systems as simple because they consist of only a few partons colliding, as opposed to the much more complex systems encountered in heavy-ion collisions

have a certain number of hard scatterings whose final state radiation is not completely dominated by the collective phenomena resulting from the QGP formation. Note that wherever one such scattering occurs, it will have at least one initial parton scattered into the QGP. The modification that the jet coming from this parton suffers due to the interaction of the parton with the QGP is what we refer to as **Jet Quenching**. Jet quenching has already been observed at RHIC[11]. However, the new energy scale accessible at the LHC and the design of the detectors operating there, will allow to study the jet quenching phenomenon in more depth, allowing us to learn about the properties of the QGP and the interactions within it.

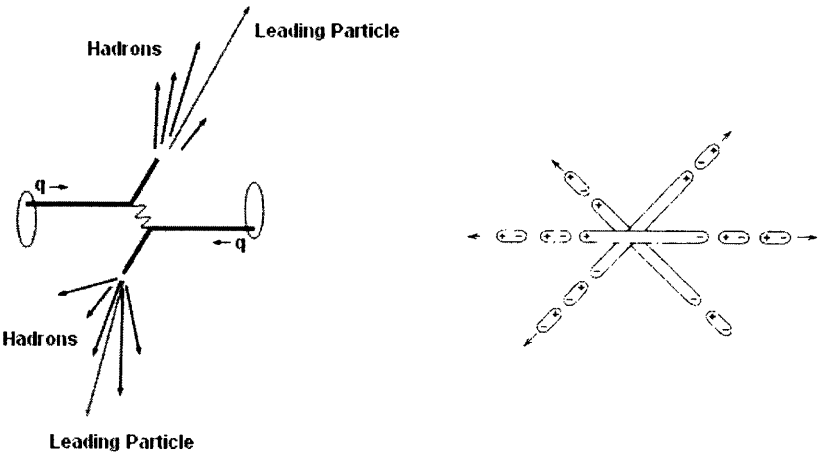

Figure 1-2: On the left: Illustration showing the interaction of two partons in a high-energy collision. The resulting particles travel in opposite directions and are located around the scattering directions of the initial or leading partons[9].On the right: Another illustration showing the process by which we obtain a particle shower from the initial parton[13]. Note that the plus and minus signs express a color charge, not an electromagnetic charge.

The goal of this thesis is to analyze the sensitivity of the Compact Muon Solenoid (CMS) Experiment to the phenomenon of jet quenching in *Pb-Pb* collisions at the LHC. To this end, we will use Monte Carlo generators which will allow us to formulate models for different quenching scenarios. In Chapter 2, we will describe the physics simulated in these generators and how we formulated the models to be used in the analyses. In Chapter 3, we will present such analyses, showing the predictions of the

different quenching scenarios about different jet observables we have identified. Also, we will analyze how these predictions are modified when background and an experimentally feasible definition of jet are added into the analyses. Finally, in Chapter 4 we will summarize and conclude our findings and discuss further work that should be done in order to fully understand the sensitivity of CMS to different properties of the QGP.

1.3 Concepts in Accelerator Physics

Before going into the next chapter, we will define a number of concepts which are used throughout this thesis and which are also commonly encountered in Accelerator Physics. These concepts will help us in the description of particle production in a collider experiment and also in the description of jets. Note that this list does not intend to be a complete glossary of terms used or defined in this thesis. Instead, it provides us with a starting set of basic concepts to work with and expand upon. Figure 1-3 illustrates some of these concepts as they relate to the geometry of a collision.

- **Beam axis.** The beam axis along which unscattered particles travel is usually referred to as $\hat{z}$-axis.

- **Transverse plane.** The plane perpendicular to the beam axis or xy-plane is what we refer to as the *transverse plane*.

- N_{coll} **and** N_{part}**.** In heavy-ion collisions we commonly refer to the number of participants, N_{part}, as the number of nucleons from both colliding nuclei involved in a collision; and to the number of collisions, N_{coll}, as the number of nucleon-nucleon collisions that occur in a single heavy-ion collision. For example, in *p-p* collisions, $N_{part} = 2$ and $N_{coll} = 1$, while in *Pb-Pb* collisions for impact parameter $b \sim 0$ (central collisions) $N_{part} \approx 406$, while $N_{coll} \approx 9N_{part}$ because every nucleon, if regarded independently, undergoes interactions with multiple nucleons in the other nucleus.

- **Geometric angles (ϕ and θ).** It is customary to use the variable ϕ to refer to angles on the transverse plane and the variable θ to refer to angles with respect to the beam axis. By definition, θ is $\frac{\pi}{2}$ on the transverse plane and 0 or π along the beam axis. The origin of ϕ in heavy-ion collisions is usually chosen according to where the reaction plane (which is defined below) is.

- **Kinematic quantities.** The center of mass of the partons involved in a scattering process cannot be assumed stationary, because each parton carries a fraction of the total momentum of the hadron it belongs to, and this fraction varies from event to event. This means that in order to study the products of such scatterings systematically, we need a way of accounting for this arbitrary boost. The way we do this is by defining particle kinematic quantities which are invariant under longitudinal Lorentz transformations, and which are therefore unaffected by this arbitrary boost. In the following quantities we use units in which $c = 1$.

  - *Transverse momentum.* The transverse momentum, p_T, which a particle may acquire through a scattering process is defined as:

$$p_T = \left(p_x^2 + p_y^2\right)^{1/2}. \tag{1.3}$$

    This is simply the magnitude of the projection of the momentum vector on the transverse plane and is Lorentz-invariant under longitudinal transformations. Its differential element is usually taken to be $2\pi p_T dp_T$.

  - *Transverse energy.* We define the transverse energy as $E_T = (m^2 + p_T^2)^{1/2}$. Note that for high-$p_T$ particles $E_T \approx p_T$.

  - *Rapidity.* A quantity which is not Lorentz-invariant but which transforms additively under longitudinal boosts and which is commonly used in the context of collider experiments is the rapidity, y, defined as:

$$y = \ln\left(\frac{E - p_z}{E + p_z}\right) \tag{1.4}$$

Because it transforms additively, the rapidity, y', of a system moving with rapidity dy with respect to some other system with rapidity y is simply $y' = y + dy$.

- *Pseudo-rapidity.* For $p \gg m$ and $\theta \gg \gamma^{-1}$, it is customary to use the pseudo-rapidity, $\eta \approx y$, defined as

$$\eta = -\ln\left(\tan\left(\frac{\theta}{2}\right)\right). \tag{1.5}$$

This quantity simply gives us geometric information about the direction of the particle and is much easier to measure in an experiment than the rapidity because it does not require the measurement of the mass. Note however that the pseudo-rapidity does not transform additively under longitudinal boosts.

- **Center of Mass Energy.** The energy scale accessible by collider experiments is often measured by the energy of the two colliding particles in the center of mass frame:

$$\sqrt{s} = \sqrt{(E_1 + E_2)^2 - (\mathbf{p}_1 + \mathbf{p}_2)^2}. \tag{1.6}$$

In symmetric heavy-ion collisions, however, it is customary to use the energy per nucleon-nucleon pair $\sqrt{s_{NN}}$. Some values of $\sqrt{s_{NN}}$ at RHIC have been 130 GeV and 200 GeV. In the *Pb-Pb* run at the LHC $\sqrt{s_{NN}}$ will be 5.5 TeV.

- **Transfer momentum.** As the transfer momentum between the two initial partons in symmetric collider scatterings occurs on the transverse plane, we usually refer to it as $\hat{p}_T$.

- **Reaction plane.** In a heavy-ion collision, the reaction plane is the plane defined by the beam axis and the impact parameter vector which joins the centers of the two colliding nuclei. We then refer to *in-plane* radiation as the particles whose momentum direction is contained in the reaction plane and *out of plane* radiation as those particles whose momentum direction is perpendicular to the reaction plane.

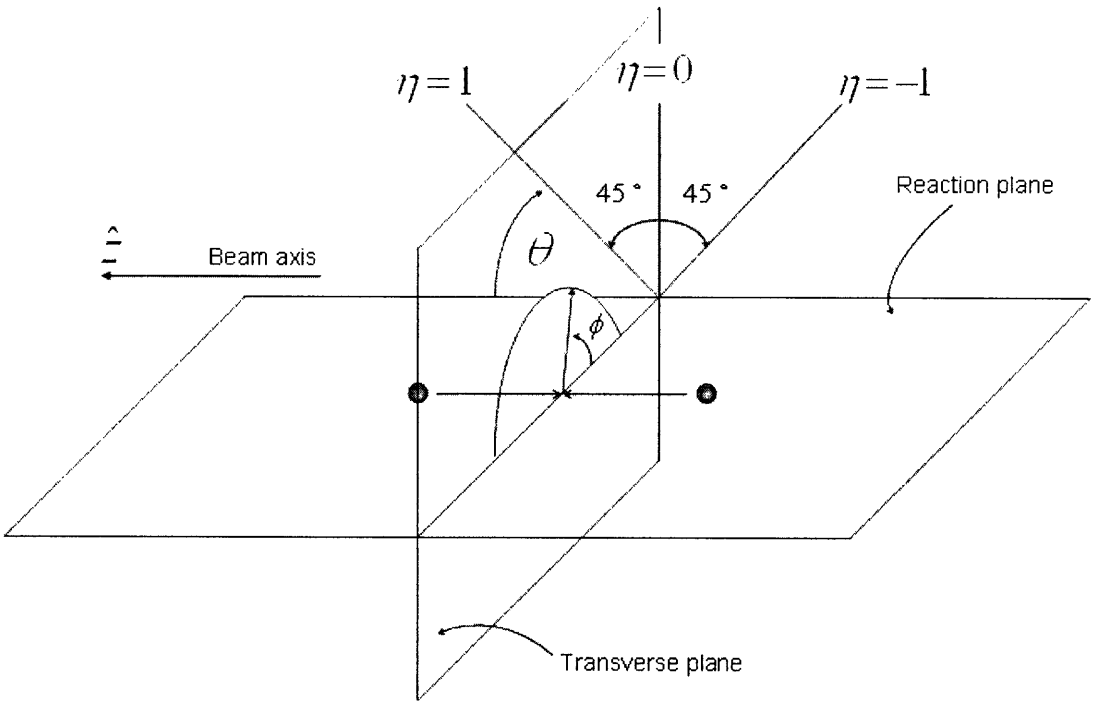

Figure 1-3: Illustration showing the geometry of a collision in a particle accelerator. For a formal definition of the different concepts in the figure please refer to the text.

- **Jet Axis.** The jet axis is the direction of the leading parton of the jet. Its coordinates are usually given in $\eta \times \phi$ space. As experimentally the information about the history of the scattering is not available, this definition is not practical. For an experimental definition of this concept please refer to Chapter 3.

- **Jet Radius.** The jet radius defines a cone in $\eta \times \phi$ space such that all the particles which were created in the fragmentation of the leading parton fall into that cone. Once more, we will modify this ideal definition to fit it to the context of the CMS experiment in Chapter 3.

Chapter 2

Theoretical Models

In the previous chapter we provided a qualitative picture of a heavy-ion collision. In that picture we identified a hot collision region where the QGP is believed to be formed, and nucleon-nucleon collisions with high momentum transfer which escape from the QGP to our detectors preserving some of the features of single p-p scatterings. In this chapter we present the more quantitative description which allowed us to simulate the heavy-ion collision through Monte Carlo generators. Attempts to accurately describe a heavy-ion collision at a wide energy range including LHC energies (with the corresponding Monte Carlo implementations) have already been made (see, for example, [22]). However, as we detail in Section 2.1, these models have been unable to mimic many of the collective phenomena observed at RHIC[14, 15]. These phenomena have a strong impact on the characteristics of the background and its fluctuations. Such characteristics fully determine the experimental resolution to different jet-quenching observables. Therefore, if we want to perform meaningful studies about the sensitivity of the CMS and the current data processing algorithms to jet quenching, it is essential to construct a model that includes the features of the data from RHIC and can be extrapolated to LHC energies.

With these motivating principles in mind, we developed a theoretical description of a heavy-ion collision which separates low-p_T and high-p_T particle production as follows:

- The simulation of low-p_T particle production is based on a hydrodynamic model, which has been largely successful to explain data at RHIC[16].

- The simulation of high-p_T particle production is based on the superposition of high-$\hat{p}_T$ nucleon-nucleon collisions. These nucleon-nucleon collisions were added using PYTHIA 6.2[17] or PYTHIA 6.2 with a quenching wrapper, PYQUEN[18], which allows us to incorporate radiative and collisional quenching effects at the parton level (we defer any further details to Section 2.2).

This theoretical description allows us to study two basic theoretical scenarios.

- In the first one we have a medium which produces no quenching of high-p_T partons but which is responsible for low-p_T collective processes. We will refer to this scenario as the no quenching scenario.

- In the second one we have a medium which interacts with high-p_T partons, quenching them and therefore causing both collective phenomena at low-p_T and suppression of the hadron yield at high-p_T. We will refer to this scenario as the quenching scenario.

In the following sections we explain the physical content of the low-p_T and high-p_T models mentioned above and how they were merged to provide a model of a heavy-ion collision based on our current knowledge.

2.1 Soft Processes and Hydrodynamic Models

We use the adjective *soft* to describe low-$\hat{p}_T$ processes. These processes are the main source of low-p_T particles in p_T spectra from heavy-ion collisions. QCD calculations of such processes are, however, not possible because the coupling constant (Equation 1.1) at low $\hat{p}_T$ (Q^2) is not small and perturbative calculations do not converge. Therefore, most of our understanding of such processes comes from phenomenological studies of data collected at the SPS and RHIC.

Before the first runs of *Au-Au* collisions at RHIC, many phenomenological models of particle production in heavy-ion collisions had been proposed to gain insight into the mechanism of such production and help in the development of the detectors and data analysis algorithms for the RHIC experiments. However, most of these models overestimated the particle multiplicities and incorrectly predicted the shapes and centrality dependences of the p_T distributions later observed[14]. More importantly, even those models which predicted the observables mentioned above reasonably well, failed completely to predict the appearance of a phenomenon known as elliptic flow[15]. Elliptic flow has been identified as a signature of the formation of the QGP in heavy-ion collisions[23] and it has been observed to be a large effect in data from RHIC[19]. This effect appears as a spatial anisotropy in particle multiplicity distributions in the transverse plane, and it reflects the initial collision geometry of the collision[20]. Figure 2-1 shows an illustration of the relationship between the collision geometry and the observed elliptic flow. The absence of this effect in the currently available Monte Carlo generators questions not only the validity of the physics models they represent but also their validity for efficiency analyses at the LHC.

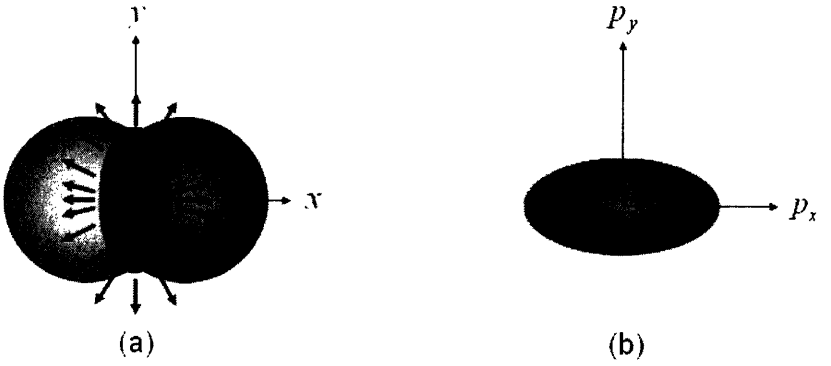

Figure 2-1: (a) The spatial anisotropy of a heavy-ion collision leading to an anisotropic particle production in the transverse plane. In this illustration, particle multiplicities would be larger in the x axis than in the y axis. (b) Corresponding transverse momentum anisotropy of initial partons before hadronization generated by pressure gradients in the hydrodynamic picture.

However, other models have been very successful at describing qualitatively and quantitatively the elliptic flow at RHIC. These are the so-called hydrodynamic models.

Hydrodynamic models consider the QGP as a thermalized hydrodynamic fluid. As such, the QGP has a thermal pressure which acts against the vacuum forcing the expansion, cool-down and hadronization (recombination of quarks to produce colorless hadrons) of the fluid. The process of hadronization creates most of the low-p_T particles detected. In non-central collisions, the elliptical shape of the collision region where the QGP is formed generates an anisotropic pressure gradient which leads to a spatially anisotropic momentum distribution in the transverse plane[21] (see Figure 2-1 (b)). In hydrodynamic models, this anisotropy in the momentum distribution of partons before hadronization is what causes the observed elliptic flow. For future reference, we will define here two concepts arising from this hydrodynamic picture which are used as the input for the Monte Carlo generator used in our analyses:

- The collective transverse flow rapidity Y_T measures the speed of the expansion of the fluid in the transverse plane, and for fixed final state particle multiplicities, it determines the slope of p_T spectra.

- The collective longitudinal flow rapidity Y_L measures the speed of the expansion of the fluid in the longitudinal direction and it determines the width of the η distributions.

However, hydrodynamic models have not only provided a qualitative and quantitative description of the mechanism of creation of elliptic flow which agrees with data from RHIC. Other observables have also been accurately described through careful hydrodynamic calculations. One such calculation compared to RHIC data is shown in Figure 2-2. A more complete analysis of the successes of hydrodynamic models in explaining low-p_T data at RHIC can be found in [16].

The close agreement of hydrodynamic calculations with RHIC data is a compelling argument to use a hydrodynamic model to describe data at LHC at low p_T in detector studies. Note, however, that the softening of the slope of p_T spectra at $p_T \gtrsim 4\ GeV$[24] has not been explained by hydrodynamic calculations. Similarly, the saturation of the elliptic flow at $p_T \gtrsim$ 4-5 GeV in 200 GeV Au-Au collisions at RHIC[26] remains unexplained in such models. Our approach to providing a model which does not

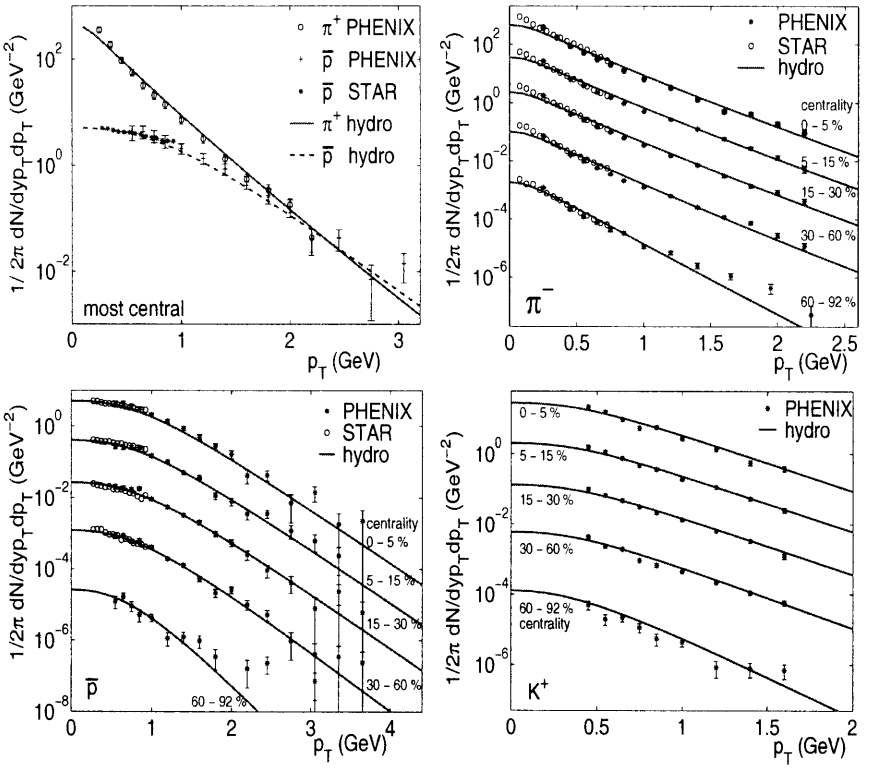

Figure 2-2: Comparison between hydrodynamic models and data from RHIC. These Figures are borrowed from [16]. The agreement between the models and the data is remarkable up to the higher p_T regions, where we can see a softening of the slope in the data which is not reflected by the hydrodynamic model.

have such strong disagreements in the high-p_T kinematic region will be the subject of Section 2.3. For now let us simply consider the low-p_T region of the spectrum at LHC where hydrodynamic models should apply if we extrapolate the behavior observed at RHIC.

In our experimental analyses, more carefully described in Chapter 3, we used the HYDRO fast Monte Carlo event generator[25], which matches this hydrodynamic description, to simulate the low-p_T part of the spectrum. Using such a fast Monte Carlo generator is advantageous because it saves computation time which is highly valuable. However, this increase in speed is achieved at the cost of increasing the number of free parameters that are input. These parameters effectively determine the hydrodynamic Equation of State and are not derived from first principles, but rather motivated by different factors which we discuss below. At this point it is worth emphasizing that the value of such a model with so many free parameters is not so

much theoretical, but experimental, because it provides us with an excellent tool based on data from RHIC to investigate the sensitivity of the detectors at the LHC.

The four main parameters controlling the physics performance of the HYDRO model are:

- Total multiplicity in central collisions.
- Width of η distributions (through Y_L).
- Slope of p_T spectra for central collisions (through Y_T).
- Type of multiplicity scaling as a function of centrality.

The motivation behind our selection of the total multiplicity in central collisions will be discussed in detail in Section 2.3. For now, it suffices to remark that we fixed it at 35000 particles for central *Pb-Pb* collisions so that the reader can understand the plots in this section. The selection of the width of the η distributions does not affect our studies very much because they are at mid rapidity. However, for future analyses at forward rapidities Y_L was chosen to be 3.75 which corresponds to a Gaussian rapidity distribution of that standard deviation. This value provides a rapidity distribution similar to that found at RHIC but scaled up to LHC predicted multiplicities (Figure 2-3 (b)). The value of Y_T was chosen to be 1.0, which corresponds to a slope of the p_T distribution matching that of RHIC data at low p_T. It has been argued that in hydrodynamics, a larger collective flow velocity will cause the slope of the spectra to be smaller at LHC than at RHIC[23]. However, this effect is incorporated into our model by adding particles coming from high-p_T scatterings as discussed in Section 2.3. Finally, the multiplicity was selected to scale with the number of participants following the trend shown by RHIC data at low-p_T[28]. Again, as we will see in Section 2.3, the multiplicity given by the final model including high-p_T contributions scales with both the number of participants and number of collisions. Figure 2-3 shows some of the basic spectra obtained with the HYDRO Monte Carlo generator and demonstrates some of the features of the model as described above.

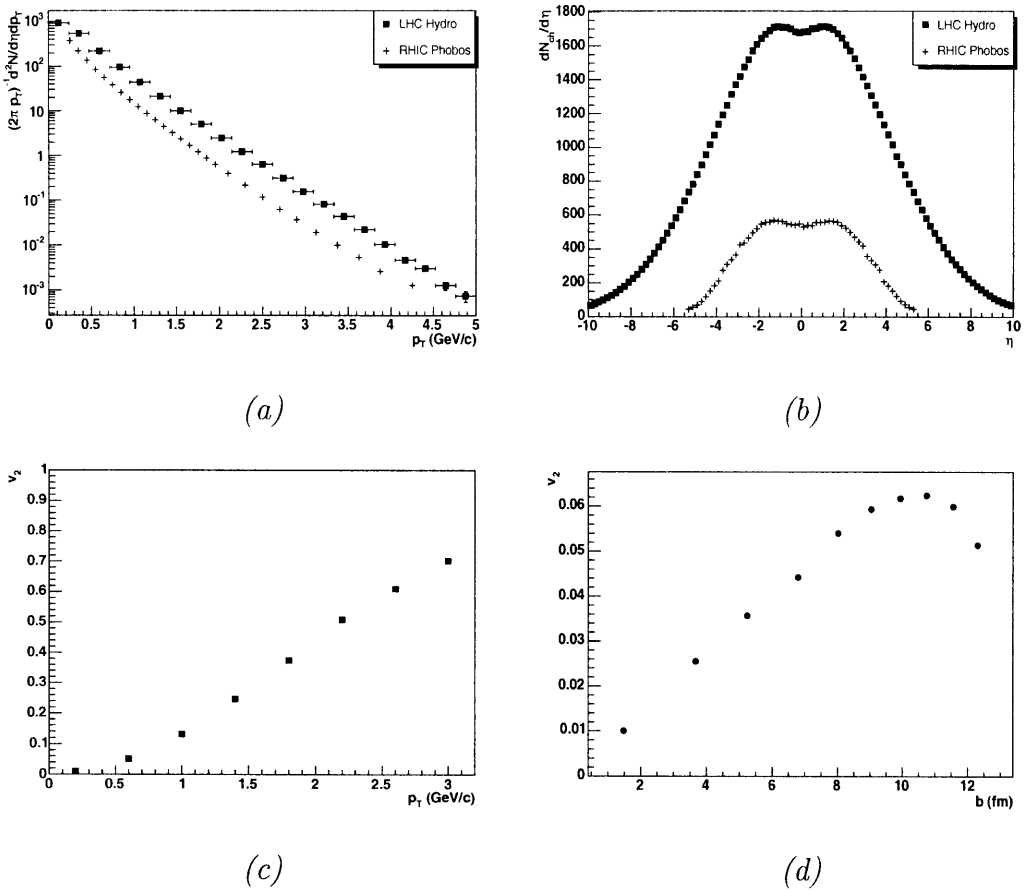

Figure 2-3: Plots illustrating the results obtained in the hydrodynamic model for low-p_T particle production at the LHC. (a) shows an average charged hadron $(\frac{h^+ + h^-}{2})$ p_T distribution per unit rapidity at η in the 0.2-1.5 range for central collisions. For comparison, data from the PHOBOS experiment at RHIC is also shown[28]. (b) shows an η distribution of all charged particles with $p_T > 200\ MeV$ for central collisions. For comparison, data from PHOBOS at $\sqrt{s_{NN}} = 130\ GeV$ is shown[27]. (c) and (d) show a quantitative measure of elliptic flow, v_2, as a function of p_T at $b = 9.93\ fm$, $\eta < 0.5$ and centrality. v_2 is simply the second coefficient of a Fourier expansion of the angular distribution in the transverse plane of final state particles $dN/d\phi$.

2.2 Jets and Models of Jet Quenching

In the previous Section we described soft processes for which QCD perturbative calculations are not possible. However, some of the interactions between the many quarks involved in a heavy-ion collision do involve a high $\hat{p}_T$. These are the so-called *hard* processes. As we mentioned in Chapter 1, the products of hard processes are highly collimated sets of particles called jets. In this thesis we are interested in QCD jets arising from processes in which we have 2 incoming partons which simply scatter from each other ($2 \rightarrow 2$ scatterings). The study of other processes such as $gg \rightarrow g\gamma$ (where g symbolizes gluons and γ a photon) which could also shed light into the mechanism of jet quenching is beyond the scope of this thesis. However, performing such studies is an important extension to the work here presented which should be performed in the future.

We also know that at the interaction scales of these processes, α_S becomes small and perturbative QCD calculations become possible. In fact, careful studies of hard processes in p-p collisions were instrumental in determining the validity of QCD in its early days. Therefore, it is not surprising that our understanding of hard processes is very good. The perturbative calculations to understand these processes are implemented in Monte Carlo generators through different methods. The one that we used in our simulations was that used by PYTHIA 6.2, known as the parton shower method. More details about this and other methods can be found in [17]. However, as the initial scattered partons separate and generate new particles in the fragmentation or hadronization process, the energy scale of the interactions becomes smaller, distances larger and once more perturbative QCD is not applicable. Hadronization models are therefore phenomenological and describe the generation of colorless hadrons from initial partons. Once more, just for reference, PYTHIA uses the so-called string fragmentation model in whose details we are not interested in here. An illustration of the PYTHIA simulation model in contrast with what happens in reality is shown in Figure 2-4 (a) and (b).

Given this picture of how a jet is generated, it seems reasonable to separate

hadronization from any in-medium interactions that partons may undergo traversing the QGP. Therefore, for simulating jet quenching, we used PYQUEN which takes the output from PYTHIA after the scattering has occurred (or the showering has happened) and then apply in-medium effects to the resulting partons before allowing them to hadronize. An illustration of the Monte Carlo steps in a hard scattering and how PYQUEN enters such sequence is shown in Figure 2-4 (c). The possibility of applying quenching effects before parton showering has not escaped our attention, and it has recently become an option in PYQUEN. However, as we mentioned above, the parton shower represents the perturbative calculation of the scattering. Therefore, it seems intuitively correct to apply any in-medium interaction after the scattering process has been fully calculated, this is, the parton shower at the Monte Carlo level has occurred. Even though the motivation for our selection does not go any further than this qualitative argument, it is of little relevance, because the measurable differences between working in one or the other scenario are experimentally negligible (see [30]). The detailed characteristics of the energy loss model implemented in PYQUEN can be found in [18]; however, let us just mention here (due to their relevance in some of the studies in Chapter 3) some key assumptions that go into the model. In particular, the model of energy loss accounts for both collisional energy loss through elastic scattering (calculated in [33, 34]) and in-medium gluon radiation as described in the BDMPS formalism[32]. The distribution of the spectrum of emitted gluons in the BDMPS formalism was taken to be Gaussian of width $\theta = 5°$ as suggested in [35]. While assuming this distribution has no stronger physical justification than others that have been proposed (see [32], for example), it already allows us to investigate some of the observable physics effects of making such assumptions.

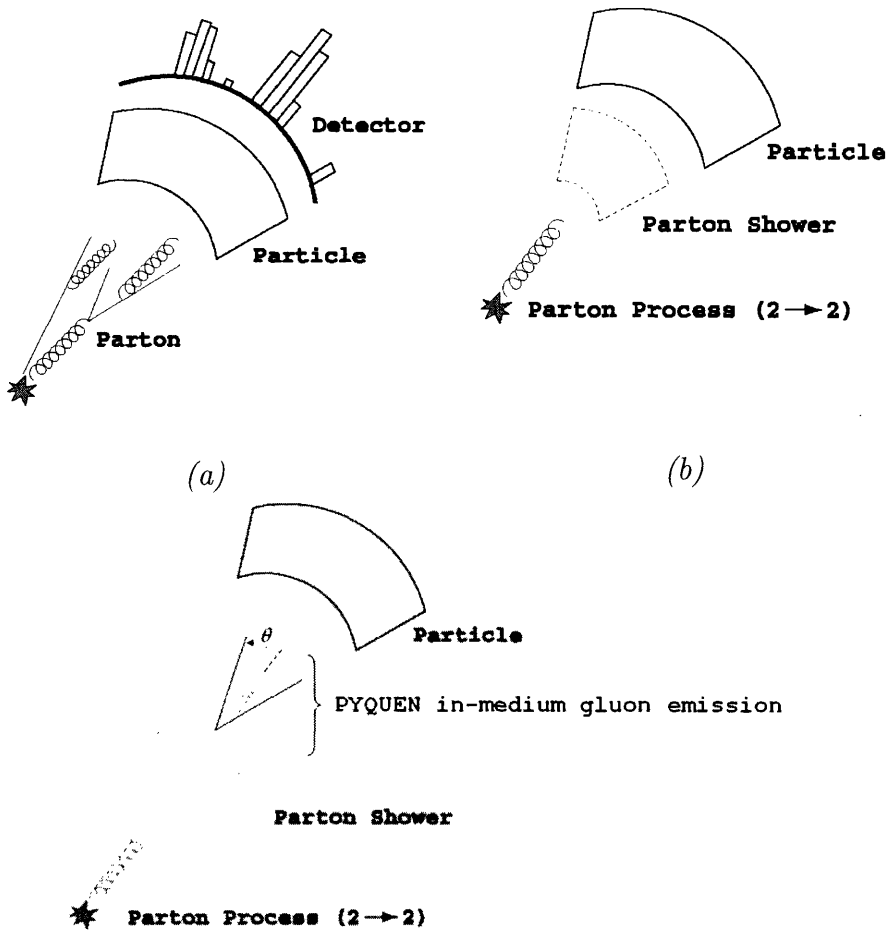

Figure 2-4: Figure illustrating the physical processes simulated in each step of the PYTHIA Monte Carlo event generator. (a) shows the scattering of the parton and generation of different partons along the jet direction and the final hadronization. (b) shows the parton shower corresponding to the QCD scattering at high p_T and the subsequent hadronization formulated using phenomenological models. Finally, (c) shows where PYQUEN introduces the medium interactions. Figures (a) and (b) are borrowed from [29].

2.3 Soft and Hard Processes: Simulating a Heavy-Ion Collision

As we have seen in Section 2.1, the agreement of hydrodynamic models with RHIC data is remarkable up to $p_T \sim 4\ GeV/c$, where the hydrodynamic description predicts a steeper slope than that shown by the data. This failure to predict data in the high-p_T range follows from the breakdown of the assumption of thermalization, which is inherent to hydrodynamic models. This is, high-p_T particles require more energy density to thermalize, and therefore they do not as we go to the high-p_T region of the spectrum or to very peripheral collisions. For this reason, it is essential for LHC studies that our model of a heavy-ion collision goes further than simply using hydrodynamics and includes the effects of non-thermalized high-p_T particles which do not follow collective phenomena.

In the picture that we have described so far, these high-p_T particles are not produced in the hadronization of the QGP but as a result of hard processes. Therefore, we can model them through PYTHIA or PYQUEN. However, we still need to determine what the meaning of hard in a heavy-ion collision is. That is, we need to determine the $\hat{p}_T$ that is necessary so that the scattered partons do not completely thermalize in the QGP. In principle, there are two approaches we could follow to answer this question. We could use the hydrodynamic Equation of State and the information we have about the energy density in a heavy-ion collision and try to calculate $\hat{p}_T$ from those quantities. The problem with this rigorous approach is that data from RHIC has not allowed us to determine either the Equation of State or the energy density with enough precision to perform such a calculation without losing all the rigor. Alternatively, we can use our current knowledge about p_T distributions at RHIC, and estimated particle multiplicities at the LHC to determine the minimum $\hat{p}_T$ that reproduces qualitatively an extrapolation of RHIC data. The lack of theoretical rigor of the latter method is comparable to, if not bigger than, that of the former one. However, we believe that the latter is of more experimental interest because the effects on the data of the different assumptions made formulating the model are easily

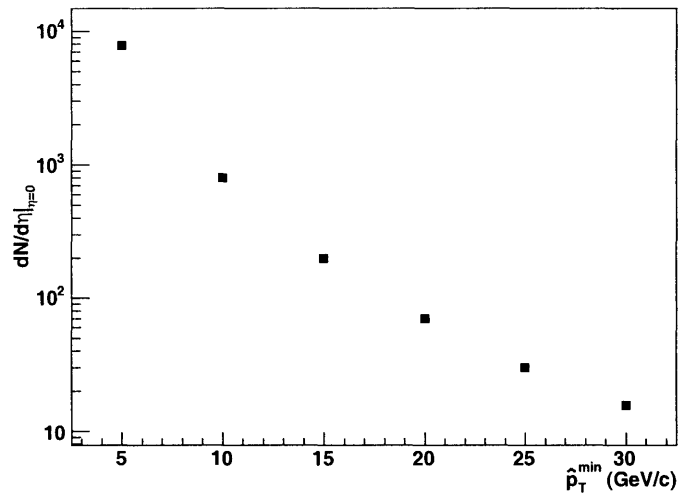

Figure 2-5: Number of charged particles per unit rapidity at mid rapidity obtained with simple collision scaling of nucleon-nucleon collisions as a function of $\hat{p}_T^{min}$. The determination of the number of nucleon-nucleon collisions given a lower cutoff on $\hat{p}_T$ was performed as detailed in the text.

predictable. This allows us to formulate a worst-case-scenario model where we can test the sensitivity of our detectors and algorithms with more reliability. Therefore, we tried to formulate such extrapolation.

The first parameter that we need to determine is particle multiplicity in central collisions. The predictions of particle multiplicities at the LHC are varied and oscillate greatly. Predictions based on participant multiplicity scaling and data from the SPS and RHIC give values of particle multiplicities as low as 1000 charged particles per unit rapidity at mid rapidity[36]. On the other hand those based on energy density calculations go as high as 3000[37]. Note that both these predictions are much lower than the ones obtained through simple collision scaling of PYTHIA events in the whole $\hat{p}_T$ range as illustrated by the low-$\hat{p}_T$ end of Figure 2-5. The number of nucleon-nucleon collisions that was used in such simple scaling for a given value of $\hat{p}_T^{min}$ was calculated using the function numjet(x) included on the HYDJET package[31]. This function essentially performs a linear interpolation between the scattering cross-sections for closely-spaced values of $\hat{p}_T^{min}$ and normalizes by an inelastic nucleon-nucleon cross-section of 58 mb as given for $\sqrt{s_{NN}} = 5.5\ TeV$ by PYTHIA. The

scattering cross-sections for fixed $\hat{p}_T^{min}$ values were obtained with PYTHIA's PYSTAT subroutine at $\sqrt{s} = 5.5\ TeV$.

As we emphasized above, it is to the interest of the reliability of our jet studies to place ourselves in a worst-case scenario where the recognition of the jets over the background becomes harder and measurements acquire more noise. We therefore decided to use a multiplicity of approximately 3000 particles per unit rapidity at mid rapidity for central collisions. If we want then to preserve any of the hydrodynamic features of the data at $p_T \lesssim 4\ GeV$ then the region with $\hat{p}_T^{min} \lesssim 10\ GeV$ must be excluded because most of the multiplicity contribution would arise from hard scatterings, leading to the disappearance of any signature of elliptic flow and an unprecedented purely collisional scaling. On the other hand, the rapid decay of hard contributions with increasing $\hat{p}_T^{min}$ creates a significant slope change in the p_T distribution as we transition from the soft to the hard regime. Such a sharp transition is not reflected on data at RHIC, where the softening of the slope occurs gradually[38, 39]. Therefore, the range of $\hat{p}_T^{min}$ where the model predicts physical results which scale from RHIC becomes very constrained to a small interval around 10 GeV. We chose to use 10 GeV which gives us a soft to hard particle contribution ratio of 2:1 approximately. This ratio gives a centrality multiplicity scaling which weighs N_{coll} scaling more strongly than the fraction observed at RHIC[16]. This is, however, expected and also desired for our worst-case-scenario approach, because it adds more fluctuations to the background from small jets, which makes jet reconstruction harder. Figure 2-6 shows basic spectra obtained with these settings with some comparisons with RHIC data. Careful analyses comparing the two scenarios are performed in Chapter 3. However, let us simply point here to the high-p_T suppression in the quenching scenario as opposed to what is observed in the no quenching scenario in Figure (a). This Figure also shows that our model predicts a softer slope than that seen at RHIC in the low-p_T range of the spectrum, as we anticipated in Section 2.1

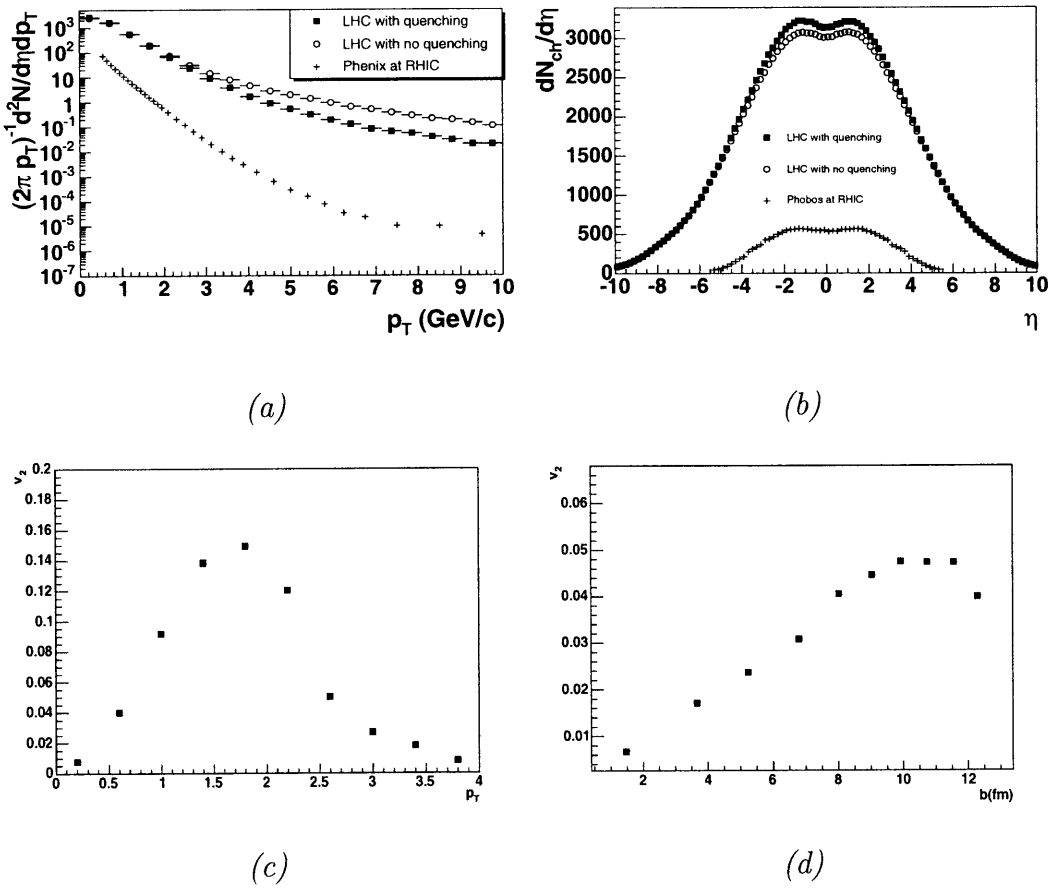

Figure 2-6: Figures illustrating the results obtained in our heavy-ion collision model at the LHC. (a) shows an average charged hadron ($\frac{h^+ + h^-}{2}$) p_T distribution per unit rapidity at $|\eta| < 0.18$ for central collisions. For comparison, data from the PHENIX experiment at RHIC is also shown[39]. (b) shows an η distribution of all charged particles with $p_T > 200\ MeV$ for central collisions. For comparison, data from PHOBOS at $\sqrt{s_{NN}} = 130\ GeV$ is shown[27]. (c) and (d) show v_2, as a function of p_T at $b = 9.93\ fm$, and centrality in the no quenching scenario for particles with $|\eta| < 0.5$. Data points for the quenching scenario in these last two plots are not shown for being within the statistical error bar of the data points shown.

Chapter 3

Experimental Analyses

In this chapter we present the different analyses that we performed using the theoretical models introduced in Chapter 2. The main purpose of these analyses is to identify observables which are significantly different between the two theoretical scenarios and to which the CMS detector is sensitive. Occasionally, we will also refer to observables which were considered but which did not show significant differences between the two theoretical scenarios. Let us emphasize here that this fact does not discard the importance of such observables at the LHC, nor does it show an inability of the CMS to study these observables. It simply shows that we may need to develop more sophisticated data analysis methods or that higher statistics may be required.

The set of analyses presented in this section can be split into two categories:

- Studies of the properties of the hadron yield at different centralities (nuclear modification factors).

- Studies of jet properties

While the methodology used for studying the nuclear modification factors is not complex, the full analyses of jet properties involve three stages with technical complications of its own:

1. Analyses of observables which are suitable at the most basic Monte Carlo level with the signal events only.

2. Analyses of jet reconstruction efficiency with the CMS calorimeter for a full heavy-ion event.

3. Analyses of the identified observables after jet reconstruction in a full heavy-ion event.

In the next section we present our results for nuclear modification factor studies and explain how we reached them. The following three sections are devoted to the three stages presented above and only Section 3.4 presents full analyses of jet observables in heavy-ion collisions at the CMS.

3.1 Nuclear modification factors

The study of the yields ($\frac{1}{2\pi p_T}\frac{d^2N}{d\eta dp_T}$ vs. p_T) at low p_T has revealed important properties of collective phenomena at RHIC[40]. However, in addition, the study of the hadron yield at different p_Ts allows us to determine where the mechanisms of particle production change and new physics is present. In order to determine where and whether such a change occurs we need some standard yield whose physics is well understood which we can use for comparison. There are currently two hadron yields that are used as standard yields:

- The hadron yield arising in p-p collisions.
- The hadron yield arising in the most peripheral heavy-ion collisions available for a specific experiment.

These hadron yields are, however, exponentially decaying functions and direct comparison between any two yields does not help much in analyzing the relevant physics involved in the particle production at different p_Ts. For this reason, the observables usually reported are the so-called nuclear modification factors R_{AA} and R_{CP} defined as

$$R_{AA} = \frac{Yield|_{AA}}{N_{coll}Yield|_{pp}} \qquad R_{CP} = \frac{N_{coll}^{peripheral}Yield|_{AA}}{N_{coll}Yield|_{AA}^{peripheral}}. \tag{3.1}$$

These definitions include a scaling by N_{coll} as defined in Chapter 1. This scaling guarantees that the nuclear modification factors are of order 1 and that we can compare across different centralities. It also evidences whether collisional scaling is present in any part of the spectrum. Occasionally, $R_{AA}^{N_{part}}$ and $R_{CP}^{N_{part}}$ have been used in heavy-ion literature, analogously. These observables evidence whether a participant scaling is present, and they have been useful for studying the yields at low-p_T at RHIC. Whether R_{AA} and R_{CP} or their N_{part} analogs will be reported by CMS Collaboration depends, thus, on the properties of the experimental data that is obtained at the LHC. However, here we are mostly interested on the high-p_T behavior where a collisional scaling is inherently present from the construction of the models described in Chapter 2, so we will only show R_{AA} and R_{CP} plots.

Given that no data for p-p collisions at LHC energies are available, the normalization used in our R_{AA} studies was obtained with over 18,000,000 simulated p-p events with PYTHIA 6.215 at $\sqrt{s} = 5.5\ TeV$. The specific settings used for this simulation provide best fits to data from CDF at Fermilab when used to simulate data at Tevatron energies. A full report of such fits and the specific settings can be found in [41]. In order to generate the heavy-ion yields of interest, we selected four different fixed centralities corresponding to the center of the cross-section bins of 0-5%, 20-30%, 50-60% and 80-90%. Note that an a-b% bin is defined between the impact parameter below which a% of the events happen and up to the impact parameter below which b% of the events happen. We determined the binnings using the HYDRO Monte Carlo which implements a standard Glauber calculation of impact parameter cross-sections for Pb-Pb collisions. A review of the Glauber model and how it is applied to calculate cross-sections in heavy-ion collisions can be found at [42]. The impact parameters corresponding to the center of the bins listed above were 1.48 fm, 6.8 fm, 9.93 fm and 12.3 fm corresponding in the Glauber model to 1814, 695, 182 and 15 binary p-p subcollisions respectively. The 80-90% yield was used to normalize the R_{CP} plots. All the yields were obtained at mid rapidity ($|\eta| < 0.5$). The R_{AA} and R_{CP} plots obtained are shown in Figures 3-1 and 3-2 for both theoretical scenarios. In these two figures the difference between the two scenarios is clearly visible. While

the collective effects and the enhancement due to radial flow at low p_T (in region (a)) can be observed in both scenarios, a strong centrality-dependent suppression appears at high-p_T (region (c)) in the quenching scenario which is completely absent in the no-quenching scenario. Note also that the change of regime is clearly observable around 4 GeV. The flatness of the R_{CP} for $p_T > 4$ GeV is a clear signature of a common mechanism for particle production at high p_T. Region (b) as marked in the figures does not reveal anything in the R_{CP} plots, but the R_{AA} plots clearly show that only hard collisions with $\hat{p}_T > 10$ GeV escape from the thermalized fluid. This effect can be observed, even in the quenching scenario, in an increasing value of R_{AA} that levels at $p_T \approx 10$ GeV. While these properties, like all the properties that we will be analyzing, are inherent to the theoretical models we used, it is important to realize that they identify high-p_T nuclear modification factors as an important window into the physics of the QGP and the different physics regimes that may appear along the p_T spectra. Current data from RHIC has allowed us to understand the low p_T part of the spectrum in terms of hydrodynamics, and a collisional scaling is expected to eventually appear at high enough p_T from hadrons that do not thermalize. These two expectations are clearly fulfilled by our model. However, the intermediate region is still not well understood. Our model simply shows that it could be a window into the momentum threshold for particle thermalization. In addition, we could expect such a threshold to be centrality-dependent. Such a dependency has not been added in our model and could in principle be used to study the phenomenology of region (b) in our plots.

It is also important to notice that the error bars in our plots are purely statistical, for we simulate at fixed impact parameter. For all practical purposes, statistical error bars will disappear for the equivalent plots in the CMS experiment. However, the efficiency and accuracy in the centrality determination using the Zero Degree Calorimeter and the cross-section binning in the actual runs will add a systematic error bar to the determination of N_{coll}. Including such an experimental error bar in our plots is beyond the scope of this thesis but should be done in the future before the first heavy-ion runs at the LHC.

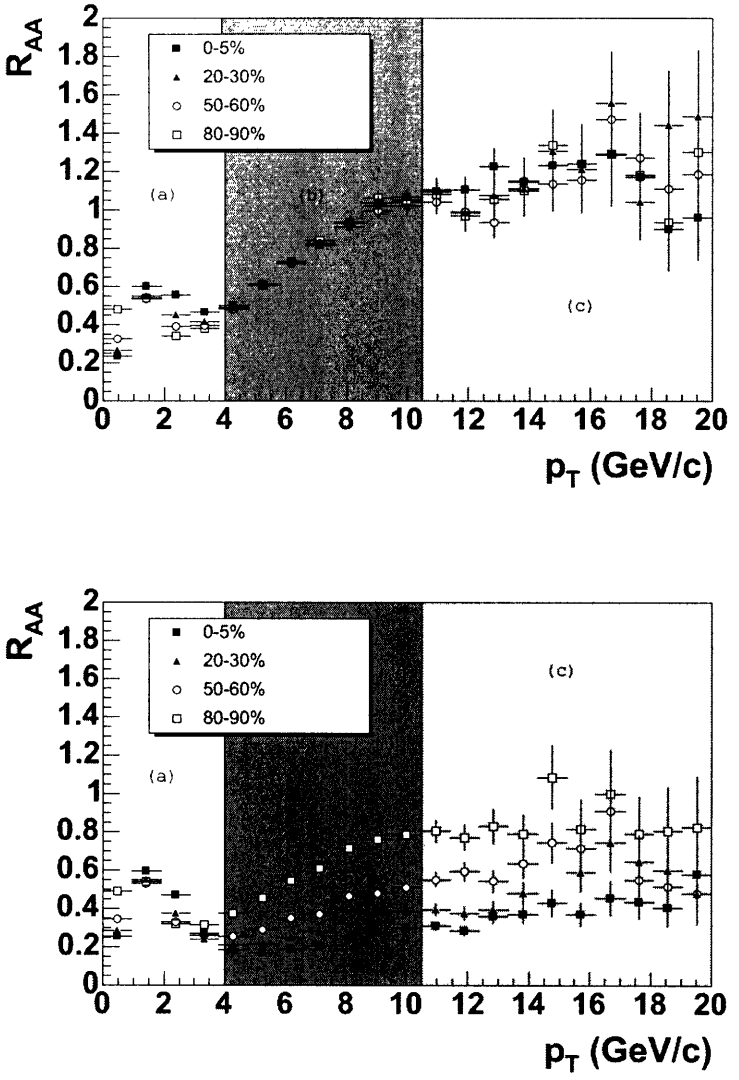

Figure 3-1: (Top) R_{AA} for the four different centralities listed in the text in the no quenching scenario. (Bottom) R_{AA} for the four different centralities listed in the text in the quenching scenario.

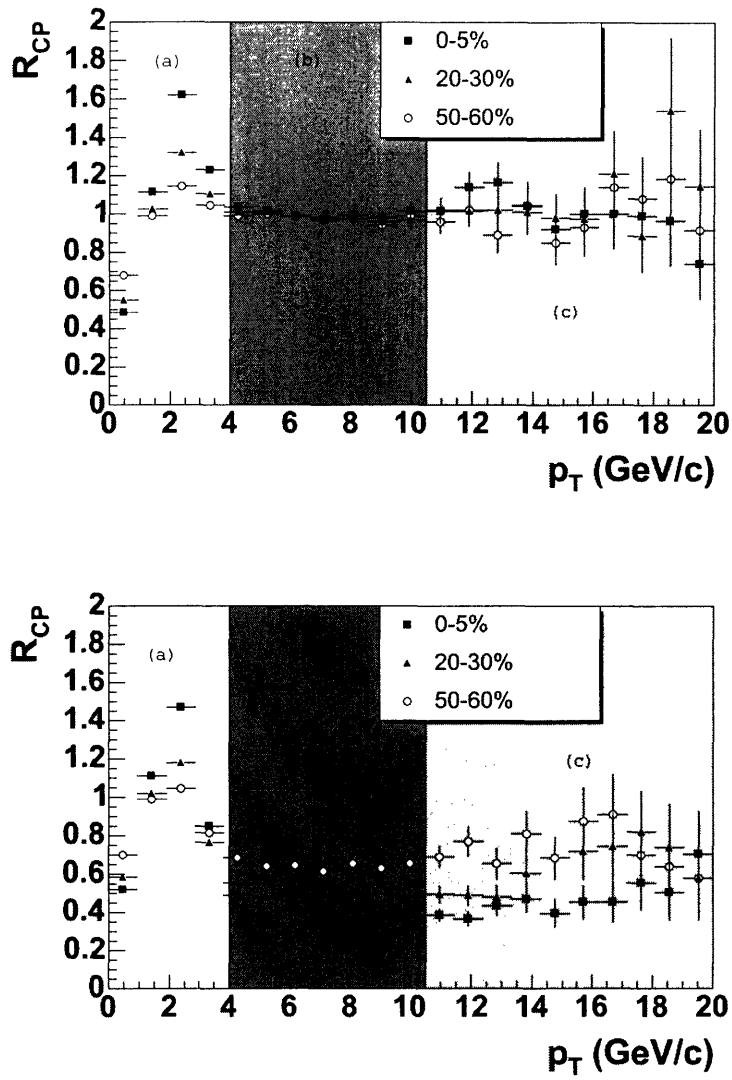

Figure 3-2: (Top) R_{CP} for the four different centralities listed in the text in the no quenching scenario. (Bottom) R_{CP} for the four different centralities listed in the text in the quenching scenario.

3.2 Jet observables

As we emphasized in Chapter 1, jet quenching is one of the promising tools which will become available at the LHC in order to study the properties of the QGP. However, the theoretical definition of a jet is not explicit enough to be useful even at the most basic Monte Carlo level. In particular, we need to define the level of collimation of a set of particles to be considered a jet. The parameterization of such level of collimation is done differently in different jet-finding algorithms. A good review of jet-finding algorithms can be found in [43]. In our analyses we use the Original Snowmass Iterative Cone algorithm because it is of simple implementation and it provides good resolution if compared to the fluctuations introduced by the subtraction of the thermal background. In iterative cone algorithms, a jet is defined as a cone of particles in $\eta \times \phi$ space. The degree of collimation is then given by the radius of this cone. Typical values of this radius are in the 0.3 to 0.7 range. While a large radius might be impractical for jet reconstruction in the presence of a heavy-ion background (as we will see in Section 3.3.2), using a too small radius may miss essential features of the jet quenching mechanism which may decollimate the jet. This decollimation effect is present in our model as can be seen in Figure 3-3. We, therefore, decided to use a cone of radius 0.5 which reconstructs almost 90% of the energy in the jet and is also usable with our algorithm for background subtraction described in Section 3.3.2.

Another parameter which enters our experimental definition of a jet is the jet energy, E_T^{jet} or the sum of the transverse energies of the particles inside the jet cone. As we will see, in both theoretical scenarios, the characteristics of the jet strongly depend on the energy of the jet. Figure 3-4 shows that this is indeed the case in p-p collisions, where the energy distribution in the jet cone is clearly different for jets with different energies. This fact, evidenced by Figure 3-4, compels a separate study of jets of different energies. We decided to study jets with energies in the ranges 50-60 GeV and 150-160 GeV. These ranges are far enough from each other to give us enough sensitivity to whatever differences are present and they are narrow enough to avoid a softening of effects arising from averaging over many jet energies.

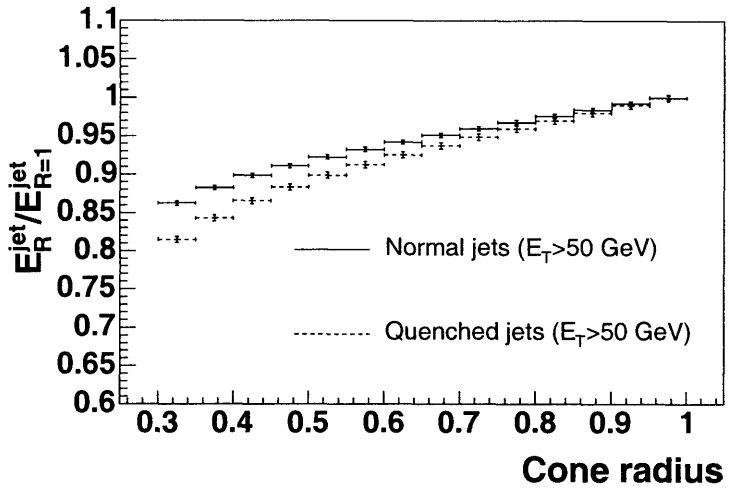

Figure 3-3: Comparison between the energy in the jet cone as we vary the jet radius with normal (p-p) jets and quenched jets. The quoted energy threshold of 50 GeV refers to the energy of the jet with radius 0.5, which was the radius used in the process of finding the jets. Note that this implies that the jets used had the same energy inside a radius of 0.5. Then we can see from this plot that the energy in the cone with R=1 was bigger for quenched jets than for unquenched jets. This clearly signals the decollimation effect mentioned in the text.

Once we have an experimentally viable definition of a jet, we need to find the objects matching this definition. As we mentioned above, we used the Original Snowmass Iterative Cone algorithm to find such objects. The idea behind this algorithm is to initially consider as jet candidates the cones around the most energetic particles, and then modify the axis of the candidate jet to account for the energy distribution inside the candidate jet cone. This procedure, which is systematically outlined below, is iterated until the jet axis is not modified by much or a maximum number of iterations is exceeded.

Iterative Cone Algorithm.

1. Consider the most energetic final state particle with coordinate (η_{max}, ϕ_{max}) and set $\eta^{jet} = \eta_{max}$ and $\phi^{jet} = \phi_{max}$. If this particle is below 1 GeV terminate. This is our jet *seed*.

2. Loop over all final state particles with coordinates (η^i, ϕ^i) and determine which

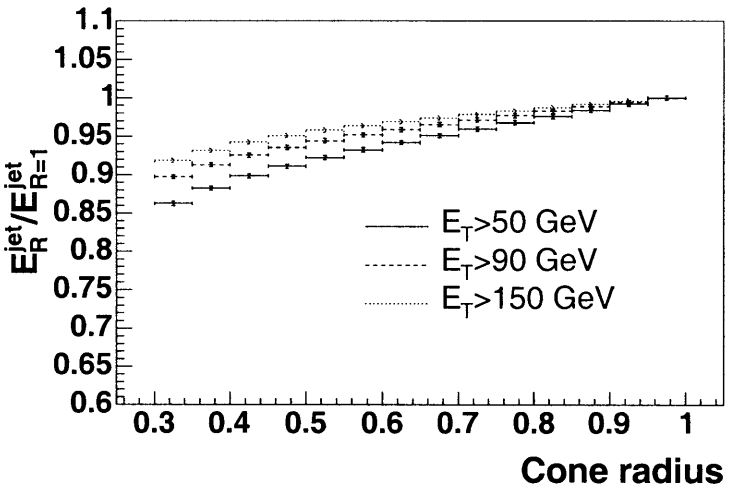

Figure 3-4: Energy inside a jet cone as a function of jet radius for jets of different energies generated with PYTHIA. This figure demonstrates that the characteristics of the jets under study strongly depend on the jet energies.

ones are inside the jet cone; that is, determine for which i's

$$\sqrt{(\eta^i - \eta^{jet})^2 + (\phi^i - \phi^{jet})^2} \leq R,$$

where R is the jet radius.

3. Use the particles inside the cone to recalculate the jet kinematic variables:

   - $E_T^{jet} = \sum_{i \in jet} E_T^i$
   - $\eta^{jet} = \frac{1}{E_T^{jet}} \sum_{i \in jet} E_T^i \eta^i$
   - $\phi^{jet} = \frac{1}{E_T^{jet}} \sum_{i \in jet} E_T^i \phi^i$

4. If $\Delta R = \sqrt{\left(\eta_{old}^{jet} - \eta^{jet}\right)^2 + \left(\phi_{old}^{jet} - \phi^{jet}\right)^2} \leq 0.01$ then remove the particles inside this jet from the list of particles, add this jet to the list of jets found and return to step 1. If $\Delta R \geq 0.01$, then return to step 2 and iterate the algorithm using the jet coordinates found in step 3. If there is no convergence after 100 steps, then remove the particles in the current cone from the list of particles and return to step 1.

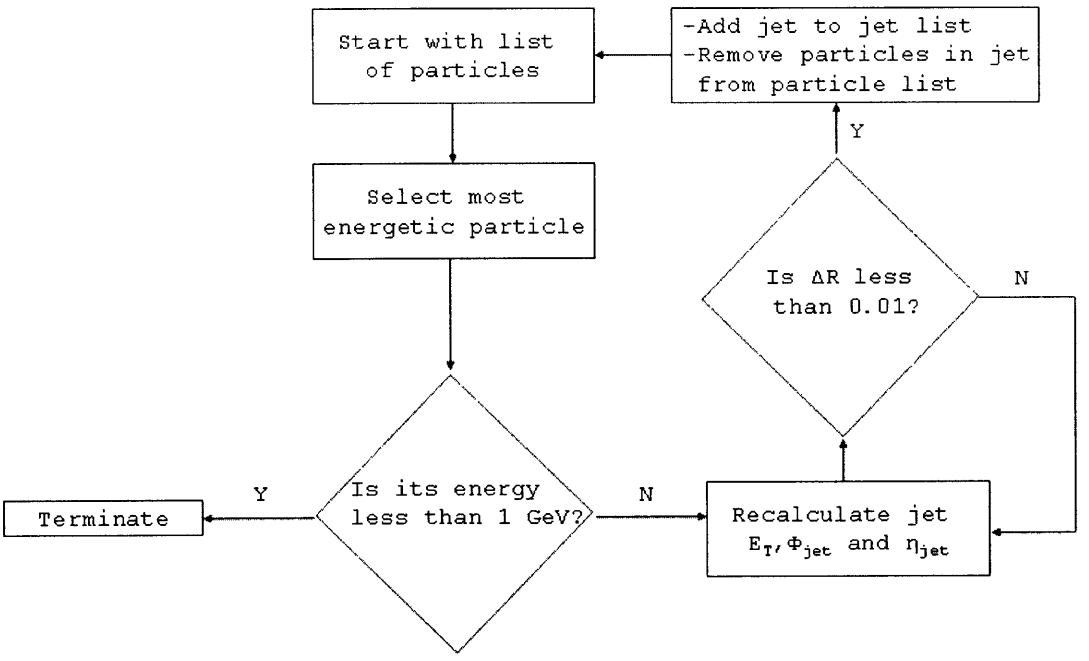

Figure 3-5: Schematic representation of the Iterative Cone Algorithm described in the text. Some of the details have been omitted for clarity.

Figure 3-5 illustrates the Iterative Cone Algorithm described above.

Now that we have given our experimental definition of a jet and described how we reconstruct jets at the basic Monte Carlo level, we can proceed and describe what jet observables we studied. Figures 3-3 and 3-4 strongly suggest that in our model there is a redistribution of the energy in the jet cone and, furthermore, that the characteristics of the jet may be energy-dependent. This motivates two fundamental analyses related to jets.

First, if we are going to perform any study of properties of jets as a function of energy, it becomes imperative to understand what the distribution of jets as a function of energy is. As we will see in Sections 3.3.2 and 3.4, this becomes even more important when experimental inefficiencies in the reconstruction of jets are taken into account. Therefore, we want to study the jet spectra in the two theoretical scenarios. A plot showing such jet spectra at the most basic Monte Carlo level is shown in Figure 3-6. The shift of the whole spectrum to lower energies in the quenching scenario is apparent in this plot. Note also how the spectra seem to get closer for higher E_T^{jet}. This could

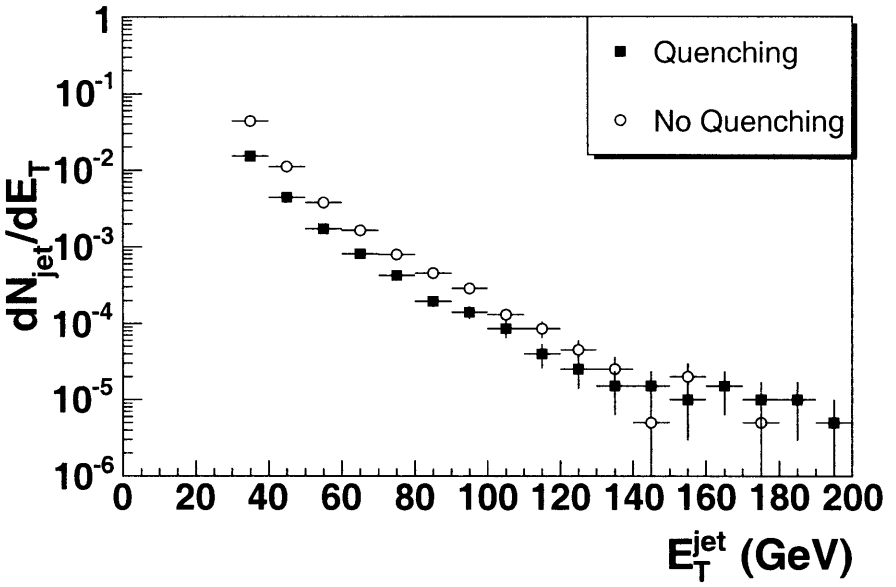

Figure 3-6: Jet spectra in the two theoretical scenarios for jets in the $|\eta_{jet}| < 1$ range. All final state particles were used for reconstructing the jet energy. This plot was obtained with 20,000 heavy ion events, in the quenching and no quenching scenarios. The jet energy threshold was set to 30 GeV to match the threshold used in the analyses in Sections 3.3.2 and 3.4

be related to the fact that the decollimation effect of the medium is stronger for low energy jets than high energy jets. This is due to gluon radiation which becomes closer to the original parton as the momentum of the initial parton becomes larger. In this hypothesis, as E_T^{jet} tends to infinity and in-medium radiation becomes more and more collinear, there should be a residual difference between the two spectra due to collisional energy loss. Nevertheless, note that this whole discussion refers to a region of the spectra for which we have low statistics. Higher statistics would clarify if the observed effect is not a result of low statistics. Also further Monte Carlo studies could be performed to confirm the hypothesis presented above.

Second, we may want to perform studies of the energy redistribution inside the cone itself. The study of such a redistribution has in fact been proposed by theorists as a possible way of learning the nature of the interactions inside the QGP [6]. Motivated by these two facts, we decided to also perform studies of the distribution of energy and particles inside the jet cone. The two types of observables we used in our studies

were *fragmentation functions* and *jet profiles*. In particular we decided to study the following four observables:

- Particle multiplicities inside the jet as a function of $z_1 = p_L^{jet}/E^{jet}$. This is the more standard form of fragmentation function. p_L^{jet} refers to the longitudinal momentum of the particle with respect to the *jet axis* and $E^{jet} = E_T^{jet}/\sin\theta$ is the total jet energy.

- Particle multiplicities inside the jet as a function of $z_2 = p_T^{jet}/E^{jet}$. Similarly, p_T^{jet} refers to the transverse momentum of the particle with respect to the *jet axis*.

- Fractional longitudinal momentum with respect to the jet axis as a function of distance from the jet axis, or p_L^{jet}/E^{jet} *vs* d in $\eta \times \phi$. This observable measures the redistribution of p_L^{jet} in the jet cone.

- Fractional transverse momentum with respect to the jet axis as a function of distance from the jet axis, or p_T^{jet}/E^{jet} *vs* d in $\eta \times \phi$.

In Figures 3-7 and 3-8 we show preliminary analyses of these observables in the two energy ranges identified above at the most basic Monte Carlo level. In such basic analyses all final state particles in the jet cone have been included without considering any detector-imposed kinematic cuts or losses in the sensitivity. Analyses including such considerations are shown in Section 3.4. These analyses were obtained with 20,000-event data sets generated with PYTHIA and PYQUEN with $\hat{p}_T^{min}$ values of 50 and 150 GeV. The number of jets within the kinematic limits imposed were between 1500 and 4500 depending on the data set. The quenching effect is clearly visible in both scenarios. However, a few comments on the adequacy of each of the observables under certain theoretical assumptions are pertinent. The jet profiles show indeed a redistribution of energy inside the jet cone. The degree of decollimation seems to be not very different, proportionally, for the two energy ranges. However, given that the original collimation as obtained in the no quenching scenario was different in the two energy ranges, a separation in jet energy bins still seems pertinent in order to

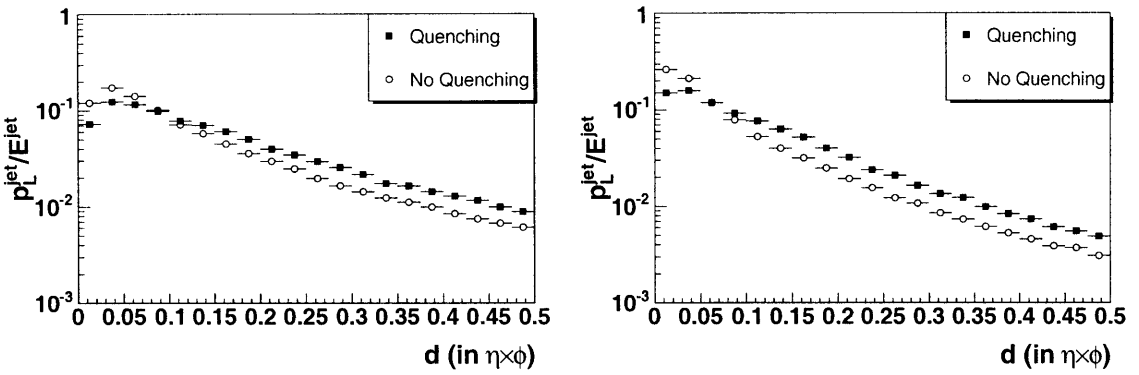

(a) *(b)*

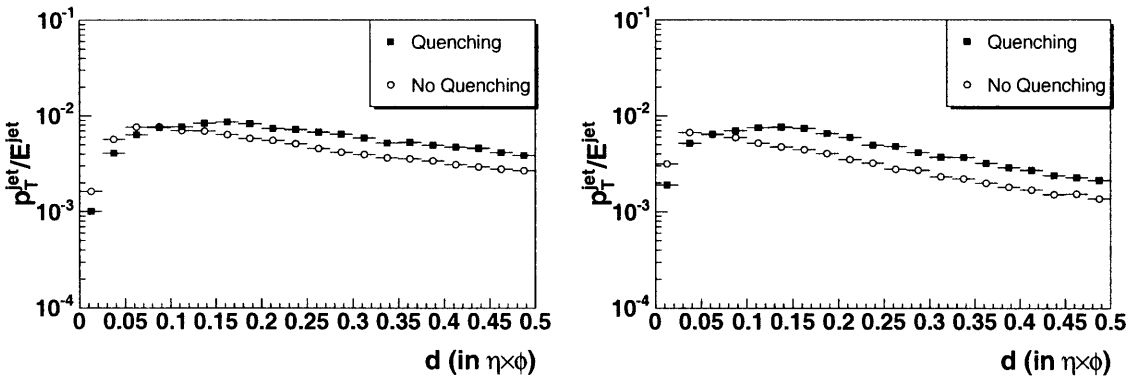

(c) *(d)*

Figure 3-7: Jet profiles for jets with $|\eta_{jet}| < 1$ in the kinematic ranges 50 GeV < E_T^{jet} <60 GeV ((a) and (c)) and 150 GeV < E_T^{jet} <160 GeV ((b) and (d)). In these plots all final state particles were used for reconstructing the jet energy and plotting the profiles.

be able to make meaningful comparisons. In addition, the p_L^{jet} plots show a strong suppression of the leading particle's momentum along the jet axis which could be subject of further study.

The fragmentation functions, on the other hand, seem to show a different response in the two energy ranges. Unfortunately, the available data does not allow us to make statistically meaningful statements about the differences at the higher z's. However, from the response of the data at intermediate z we can see that z_1 seems more sensitive to the quenching effect at low values of E_T^{jet} while for large values of E_T^{jet}, z_2 is more sensitive to the difference between the two theoretical scenarios. This could be related

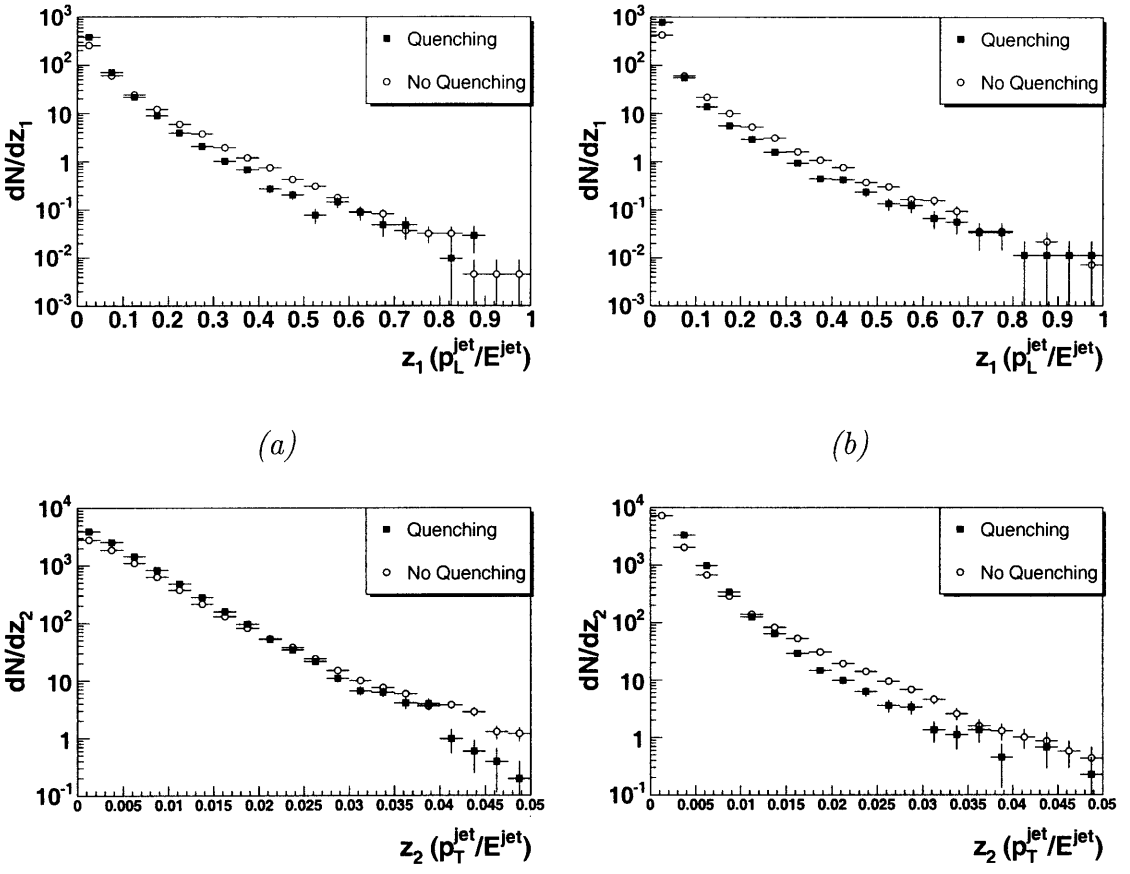

Figure 3-8: Jet fragmentation functions for jets with $|\eta_{jet}| < 1$ in the kinematic ranges 50 $GeV < E_T^{jet}$ <60 GeV ((a) and (c)) and 150 $GeV < E_T^{jet}$ <160 GeV ((b) and (d)). In these plots all final state particles were used for reconstructing the jet energy and plotting the profiles.

to a medium response which is different along the direction of the momentum of the original parton and the direction perpendicular to it and to which we definitely want to be sensitive. The study of these functions seems to provide such a sensitivity and we just need to determine now whether these features survive after the addition of background and other noise sources. We postpone these analyses to Section 3.4.

3.3 Jet Reconstruction in CMS

As we have seen in the previous section, the experimental definition of a jet in p-p collisions is not directly derived from theory, so we need to study the different observables at several energy ranges and with certain jet parameters; thus establishing an experimental definition of a jet. In addition, this definition needs to be modified to account for detector inefficiencies which, for our purposes, materialize in acceptance tables that determine which particles can be detected and which cannot. In heavy-ion collisions, where signal jets appear over a strong thermal background of collective motion and possibly mini jets, defining a jet and analyzing the effects of background noise on the different jet observables becomes an essential and inherently difficult task. In this section, we provide an introduction to the physics of the CMS detector and how different components of the detector are used for jet reconstruction in heavy-ion collisions. We also present analyses of jet reconstruction efficiency using specific reconstruction algorithms and a simplified version of the CMS calorimetry. This simplified version of the CMS calorimetry accounts for energy deposition resolution and kinematic cuts, but ignores any anomalies in the detector response in the limits of its acceptance ranges or inefficiencies of the reconstruction of charged tracks which may lead to miscalculations of energy deposited in the calorimeter. Such more complete analyses require the full machinery of the CMS simulation packages and are left to the CMS heavy-ion group as a whole.

3.3.1 The CMS detector

In order to understand how jets are found experimentally and what issues must be considered in performing realistic analyses, it is necessary to have an understanding of certain features of the design and structure of the CMS detector. A schematic of the detector is shown in Figure 3-9. Collisions occur at the center of the solenoidal magnet and the resulting particles move outwards. A strong magnetic field of intensity up to 4 Tesla generated by the superconducting coil allows the reconstruction of the momenta of charged particles with an extremely high precision in the silicon tracker.

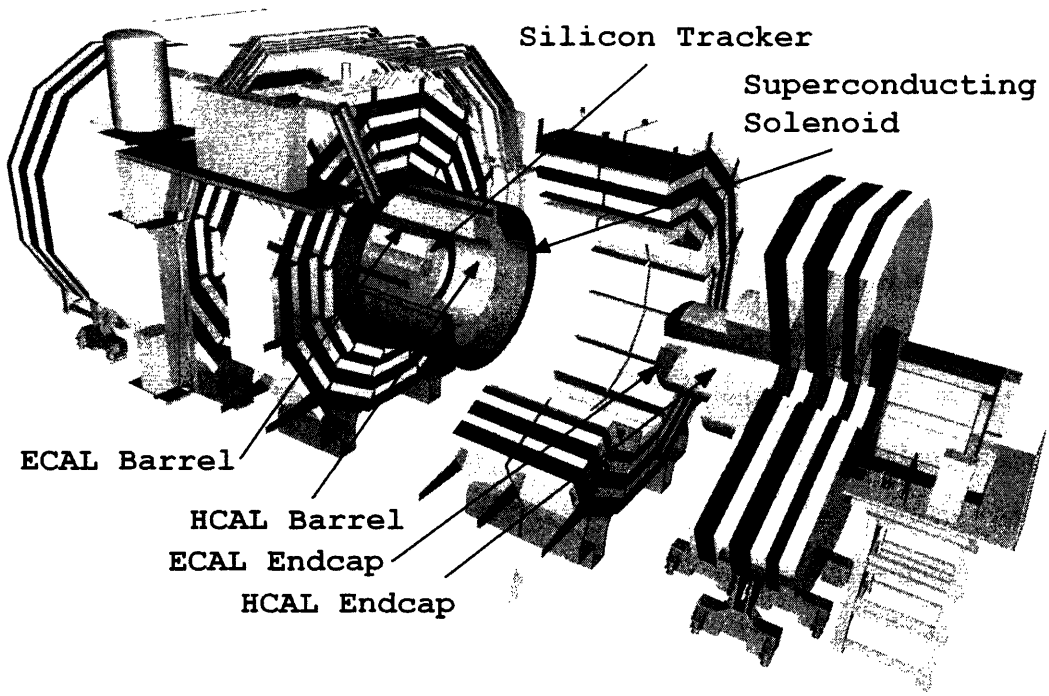

Figure 3-9: Schematic of the CMS detector. Figure adapted from [44]. The image emphasizes the location of the silicon tracker, the hadronic and electromagnetic calorimeters and the superconducting coil mentioned in the text.

However, the strong field also causes low energy charged particles with $p_T \lesssim 800\ MeV$ to bend their trajectories as much as to never reach the outer perimeter of the tracker. These particles are not reconstructible by the current track-reconstruction algorithm. Given the fluctuations of the ratio of charged to neutral particle multiplicities, it is, however, necessary to be able to observe also neutral particles in order to perform jet analyses with reliable jet energy resolution. As we saw in the previous section, the relevant azimuthal anisotropy which defines a jet experimentally is the azimuthal E_T distribution. Therefore, the determination of the individual momenta of neutral particles is not required for jet reconstruction. Instead, the use of calorimetric systems which measure energy deposition suffices. In particular, the use of a combination of hadronic and electromagnetic calorimeters, HCAL and ECAL, respectively, allows us to study the energy deposition coming from hadrons and particles which interact electromagnetically in the thermal background or in QCD jets. This calorimetric system is therefore the optimal tool for the reconstruction of QCD jets in heavy-ion

collisions. Extensive design reports of the HCAL and ECAL in CMS can be found at [45] and [46] respectively. However, let us mention here some of the features that are relevant to our analyses. The response of the calorimeter is highly non-linear for low-p_T particles allowing only the detection of a fraction of the energy deposed by neutral particles below 800 MeV. For our purposes, we ignore the energy of those particles and only account for the energy deposition of particles with $p_T \gtrsim 800$ MeV. More accurate detector simulations require the full machinery of the CMS simulation packages and are beyond the scope of this thesis. The forward and central calorimeters combined cover the $|\eta| < 5$ and $0 < \phi < 2\pi$ ranges. Our theoretical models are, however, only valid at mid rapidity. Therefore, we just need to model the barrel coverage with $|\eta| < 2$, which allows studying jets with $|\eta_{jet}| < 1$ with confidence of not losing energy due to the acceptance cuts in the η of such over-simplified model of the calorimeters. The barrels of the calorimeters are divided into calorimeter towers where energy is deposed by particles cumulatively. This leads to a granularity in the calorimeter parameterized by the tower size. This size, in the barrel, is 0.087×0.087 in $\eta \times \phi$, which results in a 46×72 tower grid and is sufficient for good jet reconstruction[45, 46]. Note that analysis difficulties arise from the energy deposed by charged hadrons whose trajectories are bent and therefore modify the original E_T azimuthal distribution. However, the information about the momenta of these charged hadrons, obtained through the silicon tracker, allows correcting for this effect. In our analyses, where the bending of the particles is not simulated, such a correction is not necessary.

Summarizing, in order to account for detector effects, we need to model the granularity of the calorimeters for jet reconstruction and use a lower acceptance cut on the p_T with value 0.8 GeV. Once such modeling is done, we need to devise a method to eliminate the background and select the jets of interest, and analyze the performance of such method in distinguishing jets from background. Such method and efficiency analyses are presented in the next section.

3.3.2 Background Subtraction and Efficiency Analyses

In order to reconstruct the axis and energy of jets in a heavy-ion collision, we need to use an algorithm that removes the background and evidences the E_T azimuthal anisotropy due to the jets of interest. The background subtraction algorithm we used was originally developed for CMS in [47]. The simple idea behind this algorithm is to obtain a better approximation to the shape of the background by ignoring previously found jets in the calculation of such shape. The shape of the background is parameterized by its average energy $\overline{E_T}$ and its dispersion σ_T. These are calculated as a function of η to account for the different sizes in η of the towers in the barrel and in the endcap and also to eliminate biases from the E_T distribution of the background along η. A systematic outline of this algorithm is shown below.

Background Subtraction Algorithm.

1. Calculate $\overline{E_T^{tower}}$ and $\sigma_T^{tower} = \sqrt{\overline{(E_T^2)} - (\overline{E_T})^2}$ for all the towers at fixed η in a given event.

2. Recalculate the energy in the towers as $E_T^{tower*} = E_T^{tower} - \overline{E_T^{tower}(\eta)} - \sigma_T^{tower}(\eta)$. If the tower energy after subtraction becomes negative, it is set to 0.

3. Using the towers with energy E_T^{tower*}, find all jets with the iterative cone algorithm described in Section 3.2.

4. Repeat step 1 ignoring any towers which belong to jets found in step 3.

5. Repeat step 2 for all towers (including those which are part of the jets found in step 3). If the tower energy after subtraction becomes negative, it is set to 0.

6. Use these towers with new energies to find the final jets using the iterative cone algorithm again.

Note that in this instance the Snowmass Iterative Cone algorithm is applied to the towers, not to the individual particles. The seeds are, thus, calorimeter towers, and the $\eta \times \phi$ coordinate of the center of the towers is used to determine whether a tower is or is not inside a given cone. The parameters that go into this algorithm are the

same that went into our original algorithm in Section 3.2, namely jet energy threshold, E_{th}, and cone radius. However, there are subtleties which must be considered when selecting values for these parameters because they can affect the identification of the background substantially. This is due to the repeated use of the Iterative Cone algorithm in steps 3 and 6. In particular, the energy threshold and jet radius that are used in step 3 determine how many towers are later used to calculate the final average energies and standard deviations. Note that, given the presence of jets, step 1 will always overestimate the average energy of the background. Then, the first run of the Iterative Cone algorithm will be done over a set of towers with less energy than the actual energy. Therefore, if we set E_{th} too high in this first run of the Iterative Cone algorithm, fewer jets than expected will be found and the second subtraction of the background will still overestimate the contribution of such background. Similarly, if we use a too low E_{th}, then too many jets may be found and the second background subtraction may happen over a too small set of towers to be representative of the characteristics of the background. A similar effect will be caused by choosing a too large jet radius. We did not perform a systematic analysis to determine the optimal parameters, and simply used $E_{th} = 30\ GeV$ and $R_{jet} = 0.5$, which have been common values used in the CMS Heavy Ion community[47]. As we will see later in this section and in the next section, such systematic studies might be key to successfully studying jet properties.

In our reconstruction efficiency analyses we used the true Monte Carlo information to determine the quality of our reconstruction. Jets found in our model of the calorimeters were matched to jets in the Monte Carlo using a proximity criterion in $\eta \times \phi$. A jet in the calorimeter is matched to the closest jet in the Monte Carlo and the match is considered valid only if their jet axes are within a distance of 0.5 in $\eta \times \phi$. Before showing these analyses, there are a few terms we need to define to quantify the quality of reconstruction, namely:

- Recognized jets. Jets in the calorimeters that are matched successfully to jets identified in the Monte Carlo.

- Not recognized jets. Jets which appear in the Monte Carlo but which were not found in the calorimeters.

- Fake jets. Jets which were found in the calorimeters but did not exist in the Monte Carlo (fluctuations in the background).

- Efficiency=$\frac{\text{RecognizedJets}}{\text{RecognizedJets+NotRecognizedJets}}$

- Purity=$\frac{\text{RecognizedJets}}{\text{RecognizedJets+FakeJets}}$

More extensive reconstruction studies could be performed in which the efficiency and purity of reconstruction are defined relative to the jet energy ranges and a fake jet is considered a jet whose reconstructed energy does not fall within its original energy range. Such analyses are, however, not the main focus of our studies and they should be performed in the future. The effects to which such analyses are sensitive were taken into account in our final analyses through our weighting procedure described in Section 3.4. We are, however, interested in the purity and efficiency as a function of the energy of the original jet because this allows us to determine the impact of reconstruction on the two different sets of analyses presented in Section 3.2. Figure 3-10 shows these two plots and two scatter plots which help us appreciate better the origin and effect of the noise that appears in the analyses presented in Section 3.4. These plots were generated from a set of 13,000 background events in the no quenching scenario. In order to improve statistics, all jets above 50 GeV were added with one event with $\hat{p}_T > 50\ GeV$ per background event. A corresponding weight to account for the different cross section of such events was added to these data points following the procedure which will be described in Section 3.4. The efficiency plots show an excellent performance of the background subtraction algorithm within our theoretical models of the background at all E_T's. However, we must realize that given our matching method, the efficiency plots are meaningless when the purity is low. This is because for low purity, so many fake jets are reconstructed that there is a high probability that a fake jet is matched with a real jet and vice versa. An improvement in the jet matching algorithm might be possible and necessary if more extensive jet

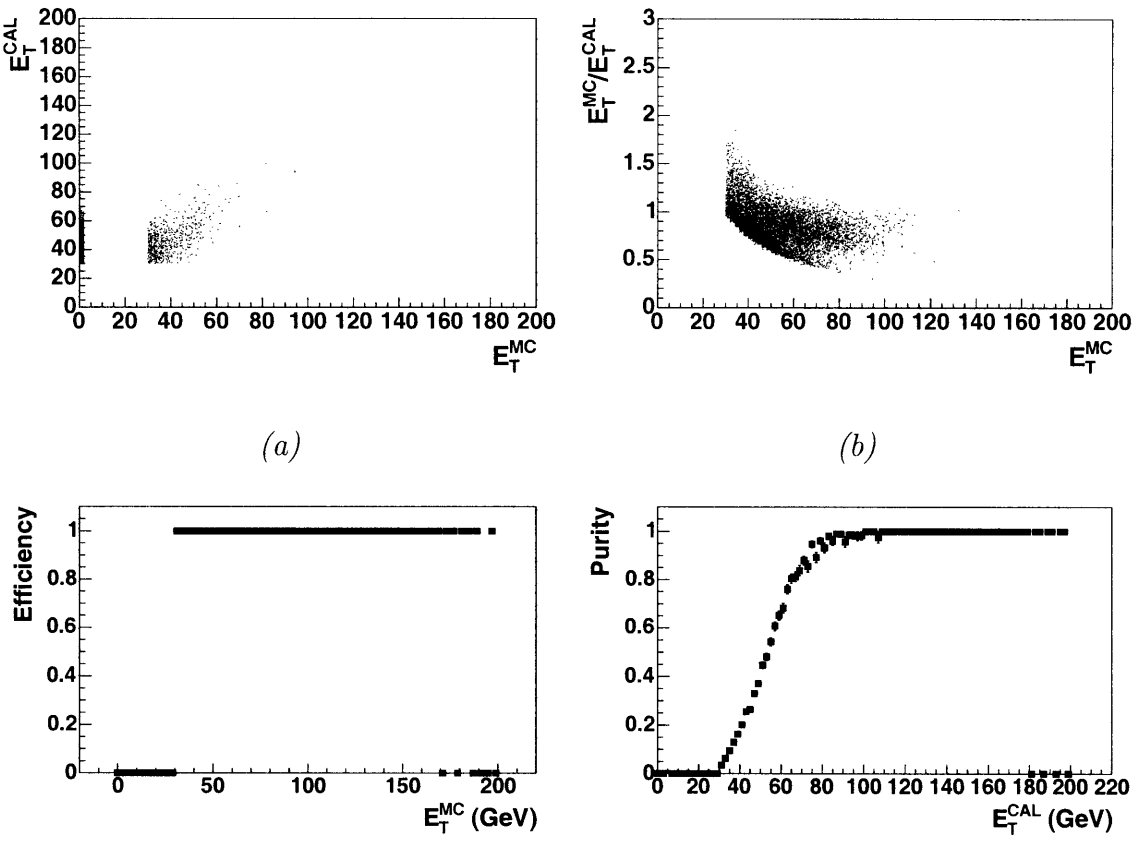

Figure 3-10: Reconstruction efficiency analyses for jets with $|\eta_{jet}| < 1$. (a) shows a plot of the energy of reconstructed jets as compared to the energy of the original jets. The points that appear near the y axis correspond to fake jets. Similarly, if there were jets that were not reconstructed they would appear as points near the x axis. The quality in the energy reconstruction is shown in (b). Finally, (c) and (d) show plots of efficiency and purity as a function of original jet energy, respectively.

reconstruction studies are performed. However, such an improvement would not allow us to identify fake jets in the absence of the Monte Carlo truth. Therefore, it would not add much to the particular studies presented here and we have, thus, not thought any further about it.

Also note that the rate of fakes is large up to $\sim$80 GeV. We therefore expect a large contamination from the background in all analyses using jets below such threshold. We can, therefore, expect our analyses with jets with E_T^{jet} in the 50-60 GeV range to be strongly affected by the presence of these fakes. How strongly they are affected

and in what sense is the subject of the next section. Note also that the energy of the jet enters the normalization of all the observables introduced in Section 3.2. As we had anticipated, it is very important that the reconstructed jet energy corresponds accurately to the Monte Carlo jet energy. Plot (b) in Figure 3-10 measures such quality of jet energy reconstruction qualitatively. More quantitatively, we calculated the average and standard deviation of $\frac{E_T^{MC}-E_T^{CAL}}{E_T^{MC}}$ as a function of the Monte Carlo true energy of the jet for the same data set. These plots are shown in Figure 3-11 and 3-12 respectively. For jets reconstructed in the ranges of interest we can look at

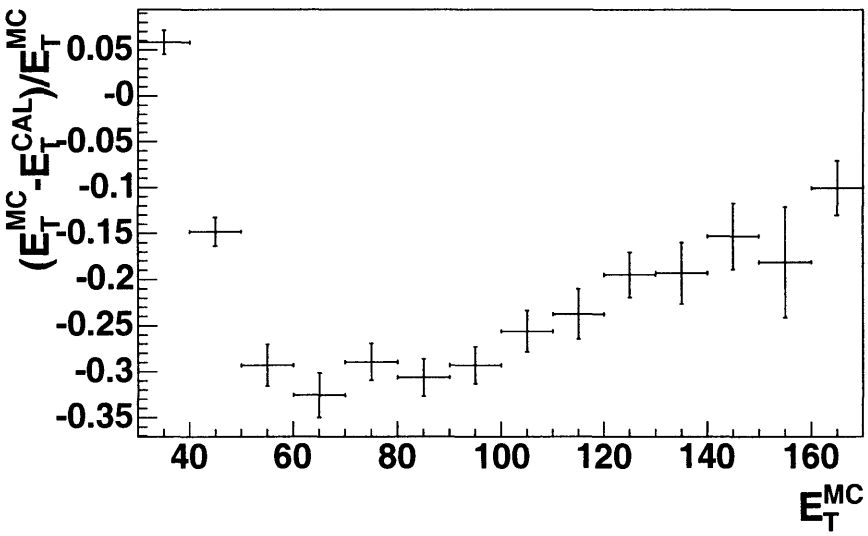

Figure 3-11: $\left\langle \frac{E_T^{MC}-E_T^{CAL}}{E_T^{MC}} \right\rangle$ as a function of E_T^{MC} for the same data set used in Figure 3-10. The errors are obtained assuming the original distributions were Gaussian. Gaussian fits to those distributions were not always good so these error bars should be understood approximatively.

the more quantitative results which can be inferred from these plots, namely:

- For 50 $GeV < E_T^{jet} < 60$ GeV: $E_T^{CAL} = (1.29 \pm 0.02)E_T^{MC}$.
- For 150 $GeV < E_T^{jet} < 160$ GeV: $E_T^{CAL} = (1.18 \pm 0.06)E_T^{MC}$.

With a dispersion σ of 0.27 and 0.24, respectively. Not surprisingly the reconstruction is better and has less dispersion for high-energy jets. While the overestimation of energy may result in a systematic error which will cancel out in the comparison of

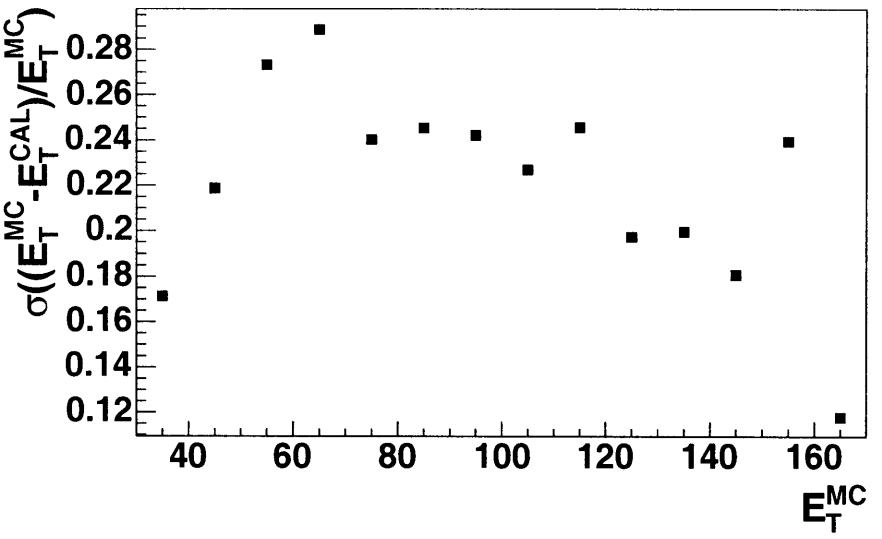

Figure 3-12: Standard deviation of $\frac{E_T^{MC}-E_T^{CAL}}{E_T^{MC}}$ as a function of E_T^{MC} for the same data set used in Figure 3-10.

two observables which are normalized by E_T^{jet}, the dispersion directly determines our resolution to differences between observables and its effect may be of a greater concern. Finally, we should realize that the jet energy spectrum is an exponentially decaying one. Therefore, any noise arising from low E_T jets which are reconstructed with a higher energy will be greatly magnified. This type of noise is present in both ranges we are using for our analyses as can be seen in plot (a) of Figure 3-10. Once more, we defer more specific comments about this effect in our different observables for the next section.

The plots and numbers just shown indicate that the jet energy is consistently overestimated. Given that less particles are used for reconstructing jets in the calorimeter due to the acceptance cuts, the only explanation to such a result is that the jet energy threshold being used is too low, so that all high energy regions of the calorimeter are ignored in the second run of the background subtraction so the average energy of the background is underestimated. This is a strong evidence showing that more extensive studies of the effects of varying E_{th} are necessary and very important if we want to have a good resolution to jet observables.

3.4 Final Jet Analyses

In this section we will put together the detector and jet reconstruction knowledge from Section 3.3 and the analyses from Section 3.2 to make realistic analyses of jet quenching, and its impact on jet shapes as detected with CMS. It is important to emphasize that given the results presented in the previous section these analyses are preliminary and should be repeated when more statistics are available and we gain a better understanding of jet reconstruction. There are, however, many useful features that we can readily see from these preliminary analyses and which we discuss in the next sections. Before getting to them, however, let us make a parenthesis to describe a mixing method which is commonly used to improve statistics when studying high-energy jets and which we used in these analyses for that purpose.

3.4.1 Mixing high-$\hat{p}_T$ and low-$\hat{p}_T$ events.

The background used in the analyses of jet fragmentations and profiles presented later in this section was either an 'unquenched' background (obtained as described in Chapter 2) for studies of unquenched jets, or a 'quenched' background, for studies of quenched jets. The background was that corresponding to collisions at the center of the 0-5% bin at $b = 1.48\ fm$. We simulated 20,000 such events and, in order to obtain better statistics for the jets in the ranges of interest, we superimposed one event from data samples with $\hat{p}_T > 50\ GeV$ or $\hat{p}_T > 150\ GeV$ per heavy-ion event. Setting such kinematic constraints in PYTHIA essentially puts a bias in what kind of events are generated, artificially increasing the cross-section of such scatterings. This means that when we add such events we artificially make our jet energy spectra more heavily weighted on their high-E_T region than they should be. This is not desirable even if we are studying jet profiles or fragmentations, because it does not consider that events at lower E_T which are reconstructed with higher E_T are in reality much more frequent than the events we are manually adding. In order to account for this higher frequency we need to weight the jets coming from the two different samples (background or signal) differently. When we do this, our statistics at high-E_T improve and the error

bars become smaller, but we preserve the appropriate weighting for different parts of the true jet E_T spectrum. Note that when we do such weighting we are assuming that all high-E_T jets come from the high-$\hat{p}_T$ sample. However, occasionally, high-$\hat{p}_T$ events may arise from the background collisions at $\hat{p}_T > 10\ GeV$. In order to do the appropriate weighting then we need to eliminate such high-energy background collisions, so that all true Monte Carlo jets in the desired energy range arise from the high-$\hat{p}_T$ sample, which is appropriately weighted.

Now, in order to do the appropriate weighting we need to know the relative cross-sections for each of the scattering processes involved. We can obtain the total cross-sections for these processes in p-p collisions with PYTHIA and they are:

$$\sigma_{\hat{p}_T>10\ GeV} = 2.7\ mb; \tag{3.2}$$

$$\sigma_{\hat{p}_T>50\ GeV} = 4.46 \times 10^{-3}\ mb; \tag{3.3}$$

$$\sigma_{\hat{p}_T>150\ GeV} = 2.6 \times 10^{-5}\ mb. \tag{3.4}$$

However, there are many p-p collisions in one heavy-ion event. This results in that ~ 90 collisions with $\hat{p}_T > 10\ GeV$ occur per central heavy-ion collision as we saw in Chapter 2. Because we have so many low-$\hat{p}_T$ events and we only add one high-$\hat{p}_T$ per heavy-ion event, we need to take this extra weighting into account. It is easy to convince oneself that the appropriate weighting to use is 1 for events coming from the background and $2.7/(N^{\hat{p}_T>10}\sigma)$ for the events that are added manually, where σ is either $\sigma_{\hat{p}_T>50\ GeV}$ or $\sigma_{\hat{p}_T>150\ GeV}$ and $N^{\hat{p}_T>10}$ is the number of collisions with $\hat{p}_T > 10\ GeV$. Figure 3-13 helps understand this weighting procedure better and demonstrates its correctness.

3.4.2 Jet Energy Spectra

Once more, we start by analyzing the jet energy spectra. Figure 3-14 shows a plot comparing the spectra in the two different theoretical scenarios. If we compare this figure with Figure 3-6 we can see that the qualitative differences between the two

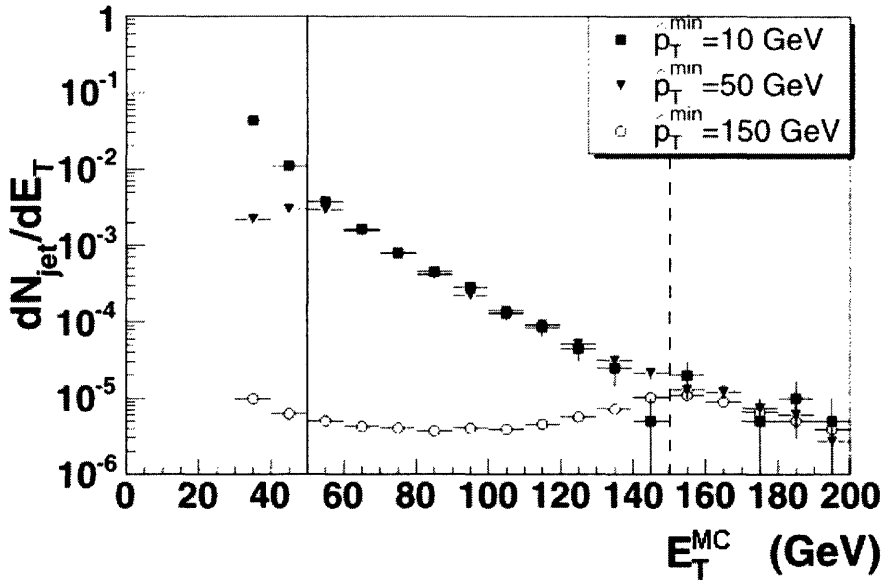

Figure 3-13: Jet spectra for Monte Carlo PYTHIA jets in a heavy-ion collision ($\hat{p}_T > 10\ GeV$) and jets we added with $\hat{p}_T > 50\ GeV$ and $\hat{p}_T > 150\ GeV$ after the weighting is applied. The solid line indicates the E_T at which we start taking events from the signal for samples where the signal has $\hat{p}_T > 50\ GeV$. All the events in the background that have a jet to the right of that line are removed from the analyses. The dashed line indicates the equivalent for samples where the signal has $\hat{p}_T > 50\ GeV$.

theoretical scenarios are preserved. However, both spectra do not approach each other in the same way as they do in Figure 3-6. The reason for this has to be found in the mechanisms of jet reconstruction. As we saw in Section 3.3.2, the energy of the jets in the no quenching scenario is overestimated probably due to a too low energy threshold for jet reconstruction. We know from Section 3.1 that the background is less energetic in the quenching scenario. That is, if the hypothesis of the too low E_{th} were true, then we would expect the energy of the jets in the quenching scenario to be overestimated less, because the high-energy regions in $\eta \times \phi$ are fewer and the second background subtraction can be done over a set of towers which is more representative of the real background. Thus, we understand this plot in terms of such hypothesis. Also we note a higher number of jets at low E_T which are simply fake jets as we can explicitly see in Figure 3-15. While Figure 3-14 may lead to think that we are very sensitive to jet quenching through jet energy spectra, we should be careful in reaching such

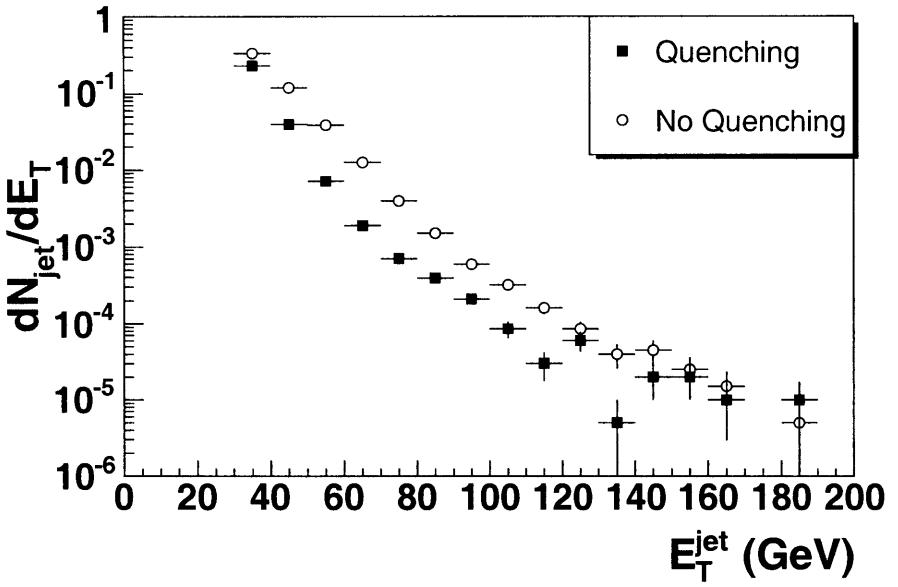

Figure 3-14: Jet spectra in the two theoretical scenarios for jets in the $|\eta_{jet}| < 1$ range. All final state particles with $p_T > 0.8\ GeV$ were used for reconstructing the jet energy. This plot was obtained with 20,000 heavy ion events, in the quenching and no quenching scenarios. The jet energy threshold was 30 GeV. Note that the label on the x axis, E_T^{jet}, refers to the reconstructed energy E_T^{CAL}.

conclusion. Given that currently there are not totally satisfactory phenomenological models of heavy-ion collisions, the question to ask ourselves is with what data we will compare the jet spectra to determine that quenching is present. If we compare it to data generated by PYTHIA, then the limited energy resolution of our reconstruction algorithms could yield a spectrum that looks like the PYTHIA spectrum. It is clear from our plots that the potential of this observable is large and that jet energy spectra will be key to understanding jet quenching at LHC. However, as we emphasized in Section 3.3.2, a good understanding of the reconstruction algorithms is essential to be sensitive to these differences.

3.4.3 Fragmentation functions

Any observable that looks at individual particles on top of a background requires a much more complex analysis procedure than the ones introduced so far because it

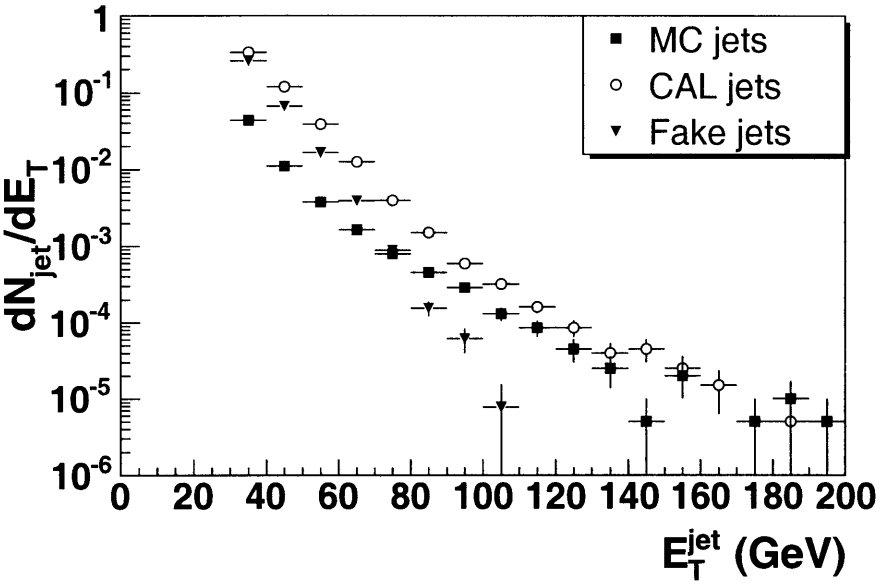

Figure 3-15: Jet spectra in the no quenching theoretical scenario for jets in the $|\eta_{jet}| < 1$ range. The spectrum of fake jets, Monte Carlo spectrum and reconstructed spectrum are shown. Note that the label on the x axis means different things for the three plots. For the Monte Carlo jet spectrum, E_T^{jet} obviously refers to the Monte Carlo energy, E_T^{MC}, while for the calorimeter and jet energy spectra it refers to the reconstructed energy E_T^{CAL}.

is not quite clear how to systematically select the particles of interest. One of the possibilities is to perform kinematic cuts to select particles which do not belong to the background with certainty. Such a selection happens naturally when working with fragmentation functions, because they simply show normalized momentum spectra. Because the normalization, the jet energy, is so large, we can be certain that the background will only appear in the lowest region of the fragmentation function, and therefore all that needs to be done is to ignore that region. Figures 3-16 and 3-17 the fragmentation functions after jet reconstruction. The first thing that might seem surprising is the similarity between z_1 in the two theoretical scenarios, which was completely unprecedented at the Monte Carlo level analyses shown in Figure 3-8. It is certainly remarkable. However, this is precisely the shift that we expect if the reconstructed energy is overestimated more in the no quenching scenario than in the quenching scenario. So exactly the same effect that caused a bigger difference

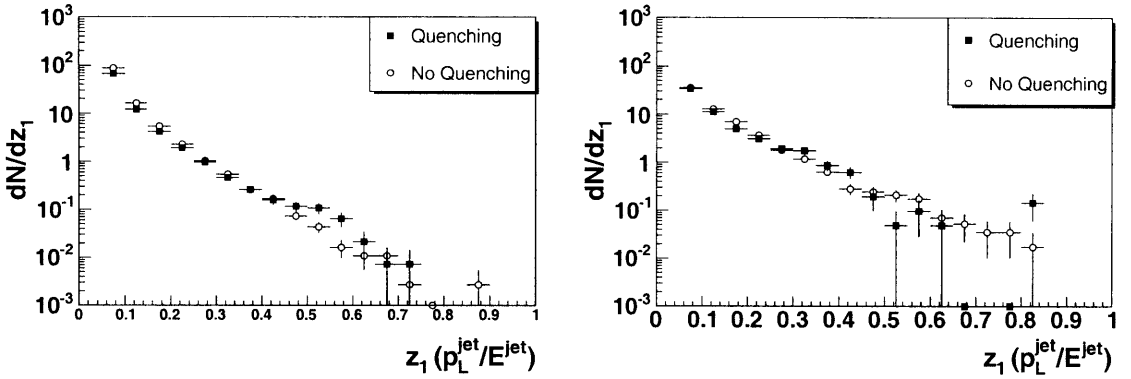

Figure 3-16: (Left) The fragmentation function z_1 as it appears after reconstruction for jets with 50 $GeV < E_T^{jet} < 60$ GeV and $|\eta_{jet}| < 1$. (Right) The fragmentation function z_1 as it appears after reconstruction for jets with 150 $GeV < E_T^{jet} < 160$ GeV and $|\eta_{jet}| < 1$. While all particles with $p_T > 0.8$ GeV were used to find the jets and reconstruct their energy, only the charged particles among them (whose momentum we can determine) were used to find the fragmentation functions. The E_T^{jet} used for determining whether a jet belongs to one of the particular energy ranges was obviously the reconstructed energy E_T^{CAL}.

between the two scenarios in the jet spectra, makes the two scenarios indistinguishable in terms of jet fragmentation functions. Once more, the importance of accurate jet reconstruction is evidenced. Note that the overestimation of energy is clearly apparent in Figure 3-16 because the leading particles, which should be there, do not appear at the high end of z_1. They have clearly been shifted towards smaller values of z_1 in the 0.5-0.7 range. In the case of z_2 we can observe an interesting effect in the lower energy range by which the no quenching and quenching scenarios are significantly different. However, comparison with Figure 3-8 shows that this is really a background effect of the types observed in Section 3.1. This is not surprising, given that in that energy range the purity of reconstructed jets is approximately 60%. Note also, that our statistics are still rather poor and that for this reason also these results are preliminary. Higher statistics are necessary in order to be able to interpret anything out of a plot such as the one on the right of Figure 3-17 and in general to be able to analyze with rigor the high end of the fragmentation functions which may provide insightful information about the effect of the medium on leading particles.

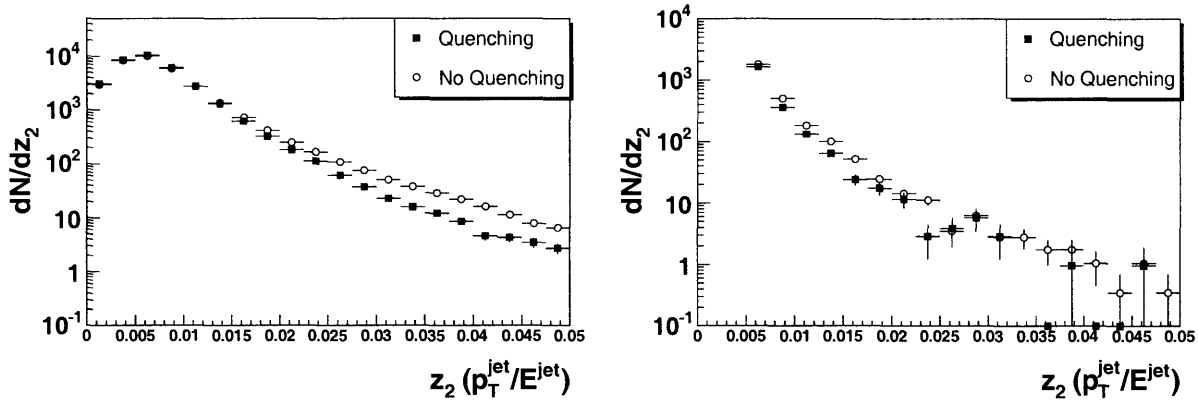

Figure 3-17: (Left) The fragmentation function z_2 as it appears after reconstruction for jets with 50 $GeV < E_T^{jet} < 60$ GeV and $|\eta_{jet}| < 1$. (Right) The fragmentation function z_2 as it appears after reconstruction for jets with 150 $GeV < E_T^{jet} < 160$ GeV and $|\eta_{jet}| < 1$. While all particles with $p_T > 0.8$ GeV were used to find the jets and reconstruct their energy, only the charged particles among them (whose momentum we can determine) were used to find the fragmentation functions. The E_T^{jet} used for determining whether a jet belongs to one of the particular energy ranges was obviously the reconstructed energy E_T^{CAL}.

3.4.4 Jet Profiles

In the case of jet profiles the challenge is bigger than that of fragmentation functions because we *are* interested in the low-p_T structure. In fact, a first question that we need to ask is whether the effects that appear in Figure 3-7 are accessible to CMS given its acceptance. Figures 3-18 and 3-19 show the two profile functions as obtained from the jets at the Monte Carlo level but only considering particles with $p_T > 0.8$ GeV for jet energy reconstruction and only the charged particles among those for filling the histograms. If we compare these figures with Figure 3-7 we can see that the interesting characteristics of the profiles are preserved after acceptance cuts are applied and only charged particles whose momentum we can reconstruct are used. As expected, the cuts are detrimental for the statistics, but the difference is not very significant. This confirms that any modifications to the profiles that may appear after reconstruction are due to the effect of the background, and not to the acceptance cuts imposed by the geometry of the CMS detector.

We can then proceed and try to determine how the background affects these

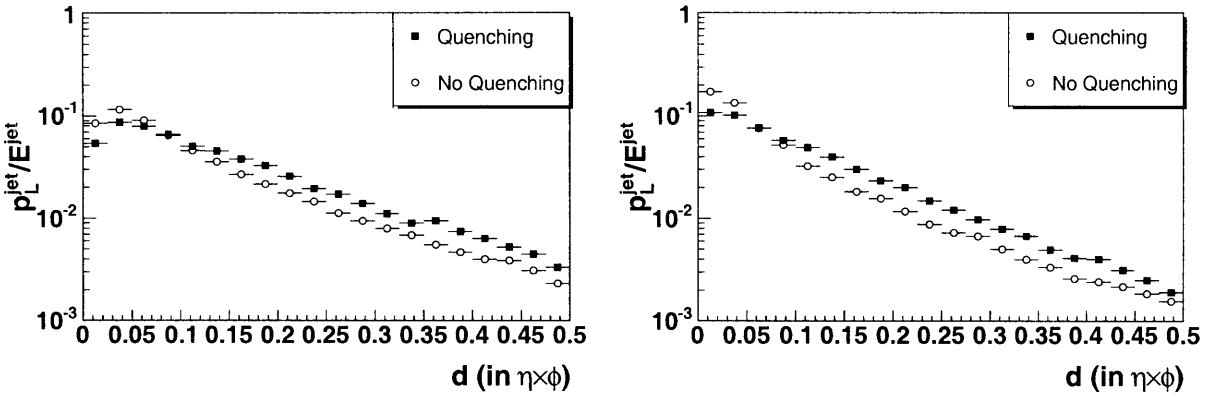

Figure 3-18: p_L^{jet} as a function of distance from the jet axis for jets with $|\eta_{jet}| < 1$ in the kinematic ranges 50 GeV < E_T^{jet} <60 GeV (left) and 150 GeV < E_T^{jet} <160 GeV (right). Jets were reconstructed using *all* particles with $p_T > 0.8$ GeV. Only charged particles with $p_T > 0.8$ GeV were considered to obtain the plots. Note how the features of the equivalent plots in Figures 3-7 3-8 are preserved if only charged particles above 0.8 GeV are used to generate the histograms.

observables. Figures 3-20 and 3-21 show the same two jet profiles for jets in the two energy ranges of interest after they have been reconstructed using the simplified model of the CMS calorimetry and all charged particles above the low p_T acceptance cut have been considered. As we can see, all the features of the profile have disappeared in the dominant background.

As an experiment, and given our knowledge of the theoretical models, we can try to eliminate all the hydrodynamic background by setting a high enough cut on the p_T and see if the desirable characteristics are recovered. Figures 3-22 and 3-23 show this exercise. In fact, we can see an effect, but an effect which does not reproduce the effect observed in Figure 3-7. Figures 3-24 and 3-25 which repeat these analyses at the Monte Carlo level show that these effects are an artifact of the background which of course is different in both scenarios once the hydrodynamic region has been ignored. This simple exercise illustrates that simple kinematic cuts may not be enough in order to analyze the more fine jet structure experimentally. The design of more sophisticated data analysis methods and the development of studies that prove their effectiveness also hold potential to be very sensitive to jet quenching given the characteristics of our profiles at the Monte Carlo level.

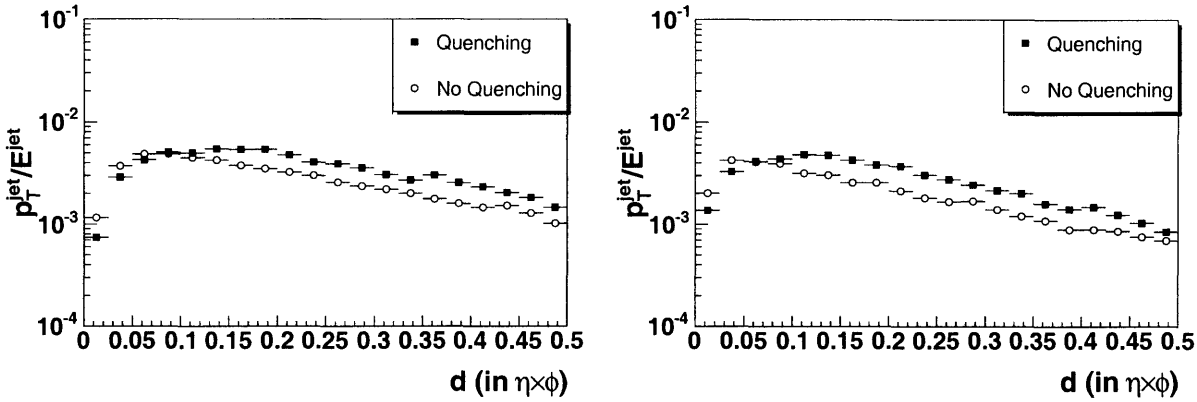

Figure 3-19: p_T^{jet} as a function of distance from the jet axis for jets with $|\eta_{jet}| < 1$ in the kinematic ranges 50 GeV < E_T^{jet} <60 GeV (left) and 150 GeV < E_T^{jet} <160 GeV (right). Jets were reconstructed using *all* particles with $p_T > 0.8$ GeV. Only charged particles with $p_T > 0.8$ GeV were considered to obtain the plots. Note how the features of the equivalent plots in Figures 3-7 3-8 are preserved if only charged particles above 0.8 GeV are used to generate the histograms.

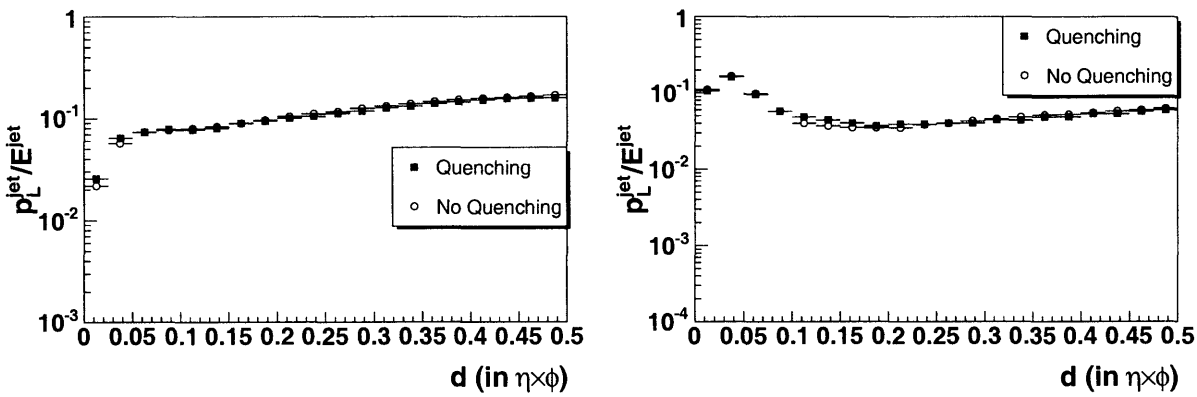

Figure 3-20: (Left) The jet longitudinal profile for jets with 50 GeV < E_T^{jet} < 60 GeV and $|\eta_{jet}| < 1$ as it appears after reconstruction. (Right) The jet longitudinal profile for jets with 150 GeV < E_T^{jet} < 160 GeV and $|\eta_{jet}| < 1$ as it appears after reconstruction. The background which increases linearly with distance from the jet axis due to the increase in area completely prevents us from being able to observe any of the features observed in Figure 3-18.

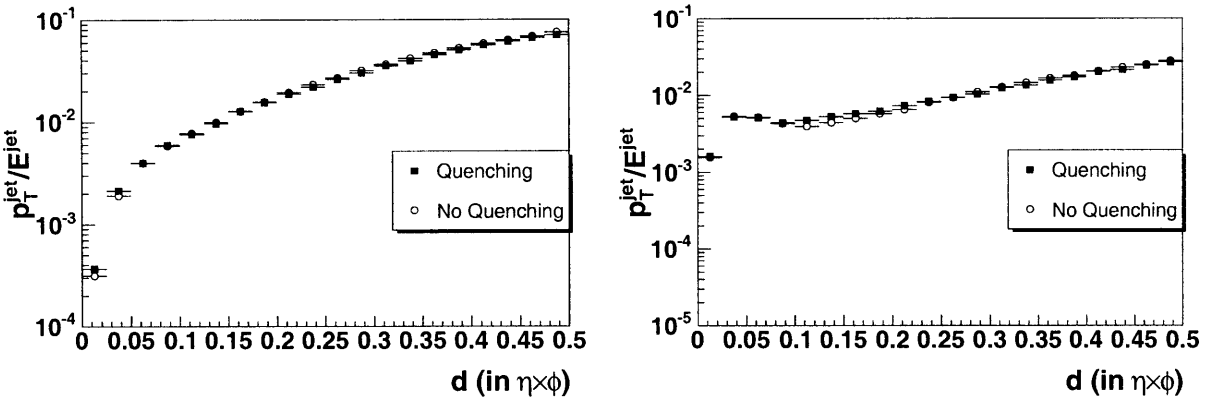

Figure 3-21: (Left) The jet transverse profile for jets with 50 $GeV < E_T^{jet} < 60$ GeV and $|\eta_{jet}| < 1$ as it appears after reconstruction. (Right) The jet transverse profile for jets with 150 $GeV < E_T^{jet} < 160$ GeV and $|\eta_{jet}| < 1$ as it appears after reconstruction. The background which increases linearly with distance from the jet axis due to the increase in area completely prevents us from being able to observe any of the features observed in Figure 3-18.

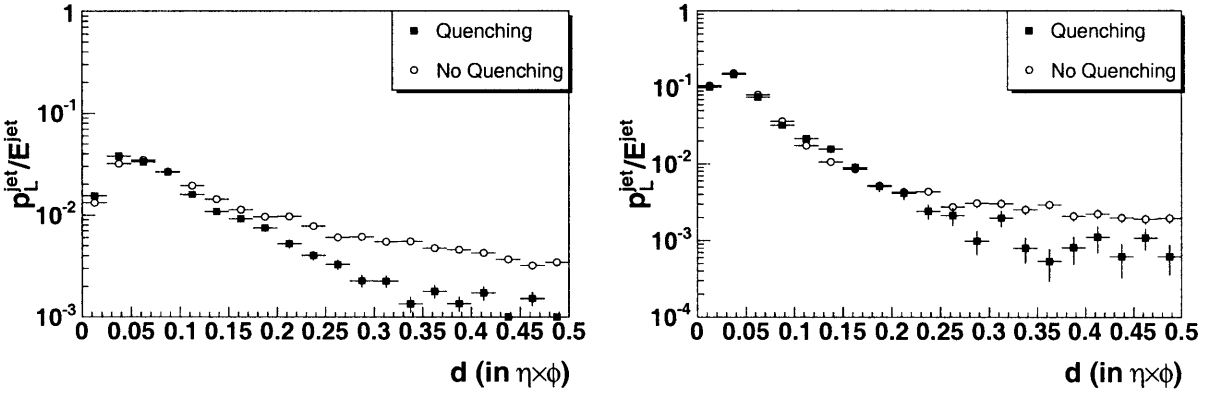

Figure 3-22: p_L/E_T^{jet} as a function of distance from the jet axis for jets with $|\eta_{jet}| < 1$ in the kinematic ranges 50 $GeV < E_T^{jet} <$60 GeV (left) and 150 $GeV < E_T^{jet} <$160 GeV (right). Jets were reconstructed using *all* particles with $p_T > 0.8$ GeV. Only charged particles with $p_T > 5$ GeV were considered to obtain the plots. This cut has been applied in light of what was observed in Figure 3-20 to eliminate the background. The difference between the two scenarios reappears, but Figure 3-24 demonstrates that this difference comes from a difference in the background and not the jets themselves.

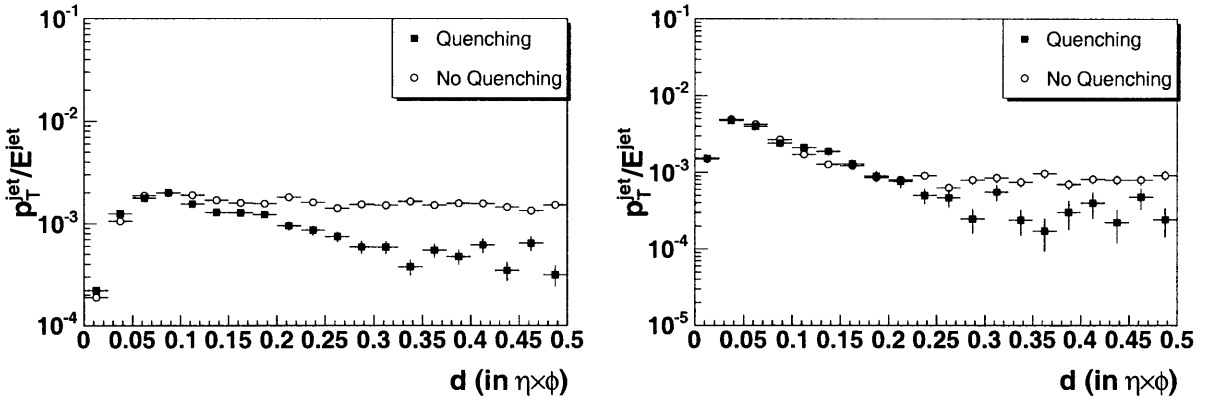

Figure 3-23: p_T/E_T^{jet} as a function of distance from the jet axis for jets with $|\eta_{jet}| < 1$ in the kinematic ranges 50 GeV < E_T^{jet} <60 GeV (left) and 150 GeV < E_T^{jet} <160 GeV (right). Jets were reconstructed using *all* particles with $p_T > 0.8$ GeV. Only charged particles with $p_T > 5$ GeV were considered to obtain the plots. This cut has been applied in light of what was observed in Figure 3-21 to eliminate the background. The difference between the two scenarios reappears, but Figure 3-25 demonstrates that this difference comes from a difference in the background and not the jets themselves.

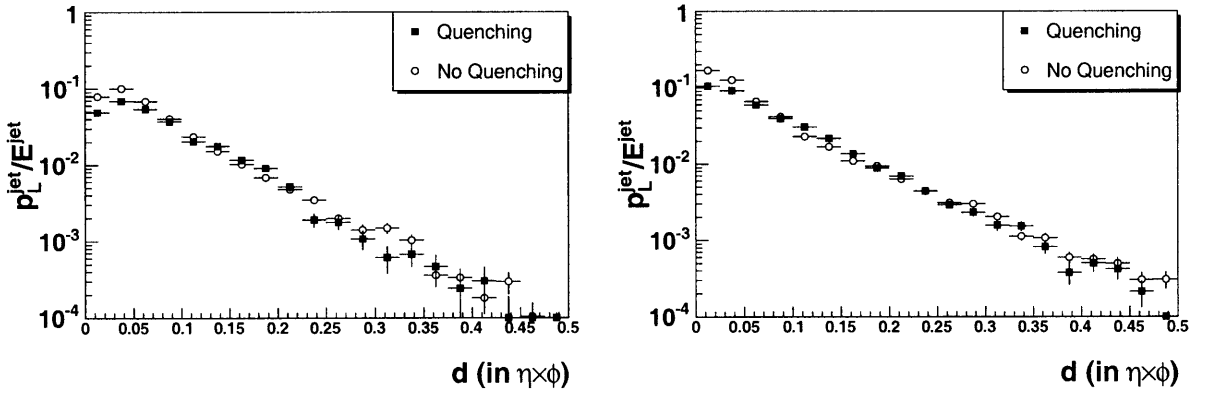

Figure 3-24: p_L/E_T^{jet} as a function of distance from the jet axis for jets with $|\eta_{jet}| < 1$ in the kinematic ranges 50 GeV < E_T^{jet} <60 GeV (left) and 150 GeV < E_T^{jet} <160 GeV (right). Jets were found at the Monte Carlo level using *all* final state particles. Only charged particles with $p_T > 5$ GeV were considered to obtain the plots.

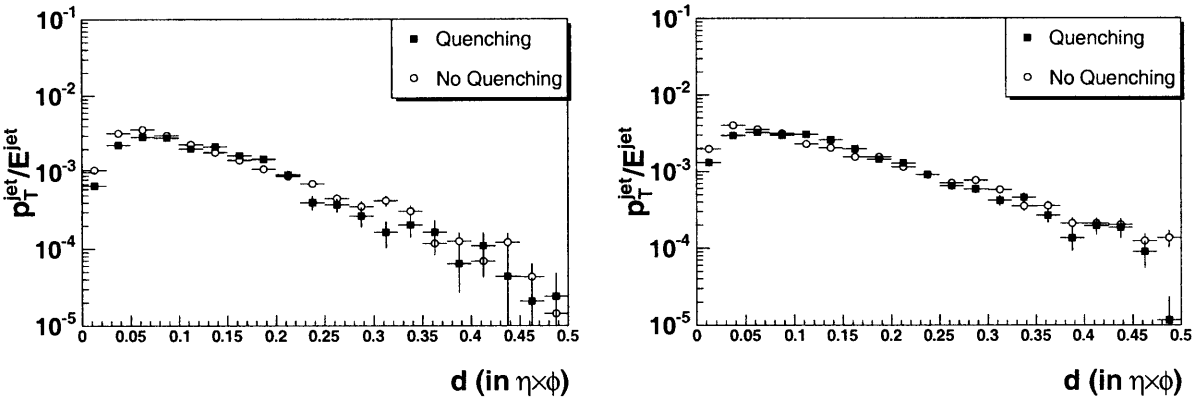

Figure 3-25: p_T/E_T^{jet} as a function of distance from the jet axis for jets with $|\eta_{jet}| < 1$ in the kinematic ranges 50 GeV < E_T^{jet} <60 GeV (left) and 150 GeV < E_T^{jet} <160 GeV (right). Jets were found at the Monte Carlo level using *all* particles with $p_T > 0.8$ GeV. Only charged particles with $p_T > 5$ GeV were considered to obtain the plots.

Chapter 4

Summary and Conclusions

In the previous chapters we have provided a description of a heavy-ion collision based on currently available Monte Carlo generators which allows users to have access to any semi-hard processes arising from the simulation of what we usually would consider the background. We have been able to test this model through many observables, some of which, such as R_{AA} and R_{CP} have given us insight into how certain model assumptions appear in the form of observables. In addition, the access to hard and semi-hard processes, has allowed us to study the features of the jet energy spectra in two theoretical scenarios where quenching of partons travelling through the medium is either present or not. These energy spectra have shown to be very sensitive to the quenching effect. In addition, we have tried to handle more complex analyses which focus on the effects of the medium in the structure of the jet. The Monte Carlo simulation of the quenching effect has proved to yield significant differences in the jet energy profiles and fragmentation functions when compared to the jets obtained in the no quenching scenario. In order to provide experimental significance to these observables in the context of the CMS detector, we have designed a simplified but fast simulation of the CMS detector geometry. While this simulation might be rudimentary, it has allowed us to perform multiple analyses and test our algorithms with a speed which makes systematic optimizations of such analyses and algorithms possible. We have used the current jet reconstruction algorithms used by the CMS Heavy Ion group and all the available Monte Carlo information to perform studies

of the reconstruction which account for the jet content of the background. These basic studies have shown a necessity to make more systematic studies of the values of the parameters entering these algorithms which should be used in order to optimize the jet energy resolution. We have, furthermore, used these algorithms to try to reconstruct the jet energy spectra and the jet structure analyses done at the Monte Carlo level. The jet energy spectra show significant differences between the two scenarios. However, we have pointed at the difficulty of finding experimentally a good standard jet energy spectrum to compare to if the jet reconstruction algorithms are not very well understood. On the other hand, many of the differences observed in the jet profiles and jet fragmentation functions disappear after reconstruction. Once again, because these observables are normalized by the reconstructed jet energy, it is essential to try to optimize the reconstruction algorithms, if any meaningful results want to be extracted from such observables. Also, the strong effects of the background have become most apparent in the jet profiles. This suggests that some other techniques for measuring the distribution of energies inside the cone might need to be considered. In addition, many possible analyses and extensions to these studies have been proposed throughout the text.

Summarizing, we have shown how considerations of jet reconstruction and jet energy resolution will be essential to detect jet quenching at the LHC. We have also shown how the characteristics of the CMS detector make it optimal for such studies. However, we have also insistently pointed out that a better understanding of the detector and jet reconstruction algorithms is required if the full capabilities of CMS for jet Physics want to be exploited. While this thesis has introduced some rather basic analysis procedures and observables, we hope that they serve the CMS Heavy-Ion community for further development of more sophisticated techniques which lead to an exciting and successful program in jet Physics with CMS.

Appendix A

The data analysis framework: CMSROOT

The analyses presented in this thesis required the manipulation and storage of large amounts of data in a similar way to how data will be processed once the CMS experiment starts collecting them. The CMS Collaboration already has developed software in order to perform detector, reconstruction and physics simulation studies. However, modifications to this software are not easy to implement. In particular, at the time of completion of our analyses, this software did not support the use of the Heavy-Ion specific generators that were used in this thesis. We developed CMSROOT in an effort to provide a flexible generic data-analysis framework which can be used for fast Monte Carlo studies by the CMS Collaboration. In the following pages we clarify these goals by defining a set of precise specifications and explaining how these were implemented, emphasizing details that are relevant for further development of the framework. Let us emphasize here that CMSROOT is a rapidly-evolving framework, and, as such, the content of this report will eventually be outdated. This report is therefore mostly targeted to people interested in the design considerations that went into the original development of the framework, and focuses on the aspects of it which we envision will not change significantly during its evolution. For specific user questions please refer to the updated examples in the CVS repository for CMSROOT[1].

[1]For access please contact Maarten Ballintijn at maartenb@mit.edu

A.1 Design Overview

The handling of large amounts of data for the purpose of High Energy Physics research is not a new problem, but rather one which every modern High Energy Physics experiment faces. However, the unique characteristics of each experiment require different features from the analysis tools and, therefore, the frameworks need to be redesigned every time to adapt to the new requirements. Nevertheless, a set of basic tools for histogramming and generic data manipulation which was originally developed and continues to evolve at CERN has acquired popularity among the High Energy Physics community. This set of tools, from which CMSROOT derives its name, is known as ROOT[48]. CMSROOT is built on top of ROOT and therefore a basic knowledge of ROOT is assumed throughout this document. For specific user questions about ROOT please refer to [49].

The design of a general-purpose system such as CMSROOT entails difficulties arising from a lack of well-defined requirements and the flexibility and simplicity which must be preserved when adding modules. These two considerations drove our design. The first one compelled us to define a model that mimics the data flow in an experiment as shown in Figure A-1. The second consideration influences the design and implementation of every module and we will refer to it when discussing specific modules.

Figure A-1: Data flow in a general-purpose data analysis framework. In such framework, modules representing the three data creation, storage and access or analysis must be provided. 1 and 2 correspond to interfaces between these modules.

The original set of requirements were the following:

1. Provide an easy-to-use interface to Monte Carlo generators of heavy-ion collisions for the creation of simulated data.

2. Allow for efficient and easily accessible data storage.

3. Create easily expandable data analysis classes.

As already noted above, these points represent a direct translation of the natural data-flow chart of Figure A-1 to specific design goals. However, addressing them requires more specific considerations which account for the available resources (the Monte Carlo generators and ROOT). In particular, Monte Carlo generators are usually implemented in FORTRAN where common-blocks maintain the state of the generator. To be able to integrate such code in a C++-based framework such as CMSROOT we used CFORTRAN[50], which allows us to translate common-blocks to C++ `structs`. Each generator is then represented by a class derived from `TCMSGen` which has access to these common-blocks.

Also, the last two points have received attention in ROOT, which provides a `TTree` data structure for efficient data storage and a `TSelector` class which interacts with `TTree` objects for easy access to the data. While these classes are still too generic to fully address the last two points, they provide a starting point from which we can develop a solution. In fact, all that we need to do is to use a `TTree` object with a specific format defined for CMSROOT and to access it through a `TCMSSelector` which inherits the desirable properties of the `TSelector` and hides the details of our particular storage format. The specific format makes use of classes defined in CMSROOT for particle representation and event information storage. The details of the creation of a `TTree` in CMSROOT format are encapsulated in a tree-maker class, `TCMSAnalysisTree`, which serves as an interface between the output of the generators and the data storage in `.root` files. A schematic showing the structural overview of CMSROOT we have just introduced is shown in Figure A-2. In addition, for the purpose of the analyses presented in this thesis, we added many data analysis classes to the framework. The addition of such classes was straight-forward due to the design and functionality of the `TCMSSelector` class. However, it will not become obvious to the reader how such design aids in the addition of new analysis classes until we show the details of the implementation and usage of the `TCMSSelector` class. We postpone

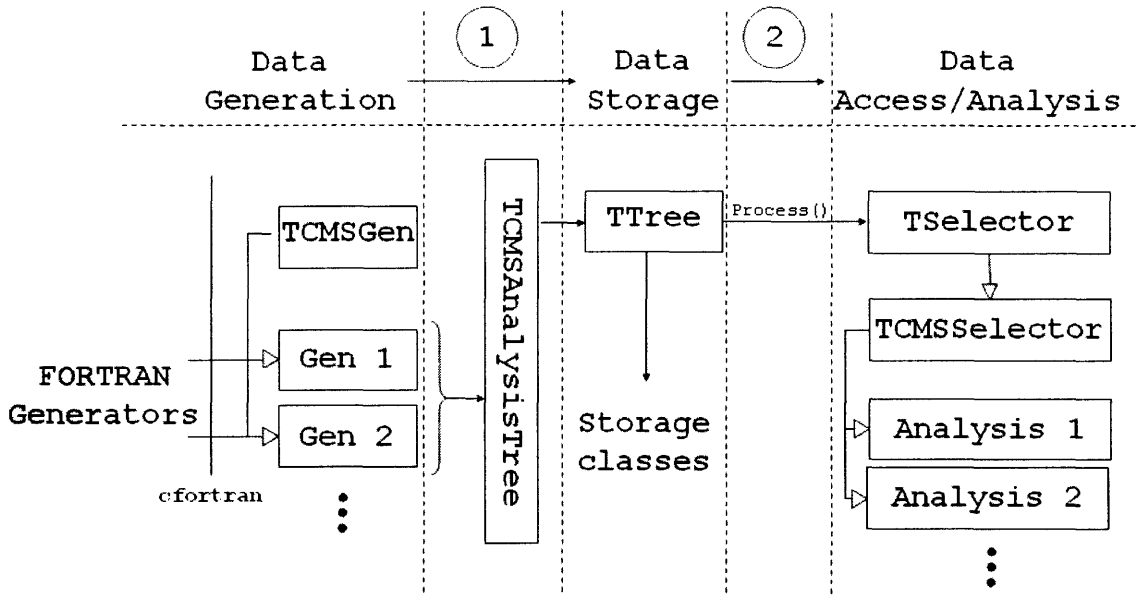

Figure A-2: Structural overview of CMSROOT, specifying different modules, their interactions and their function as it relates to the overall data flow specified in Figure A-1.

such detailed description to Section A.2.3. Note here, though, that this aspect of the `TCMSSelector` addresses items 2 and 3 in our list of design goals.

A.2 Design Description

The previous section outlined the main components and their interactions within CMSROOT. However, any further development requires a more precise knowledge of those components and the many subcomponents that form them. A detailed description of the implementation and interaction of these modules is developed through the next sections.

A.2.1 Data storage

The data storage classes constitute the backbone of CMSROOT and are located in the `base` and `tree` shared libraries. The `base` shared library contains the essential structures for storing particle information: `TCMSParticle` and `TCMSVertex`. The structure of these classes is shown in Figure A-3. Access to the member fields is provided. This

```
class TCMSParticle::public TObject
{

private:
   TRef           fStartVertex;
   TRef           fStopVertex;
   TVector3       fP;      //momentum
   Int_t          fPID;    //particle id
   Int_t          fStatus; //status code

public:
      .
      .
      .
}

class TCMSVertex::public TObject
{
private:
   TVector3       fPos;
   TRefArray*     fDaughters;//Array of ROOT pointers to daughter particles
   TRef           fMother;   //ROOT pointer to mother particle

public:
      .
      .
      .
}
```

Figure A-3: Stubs for the classes `TCMSVertex` and `TCMSParticle` representing decay vertices and particles respectively.

allows reconstructing the a tree representing the event history where `TCMSVertexs` represent the decay vertices and `TCMSParticles` represent the particles involved in the decay. This reconstruction can be performed using the references to the start and stop vertices in `TCMSParticles` and the mother and daughter particles in `TCMSVertexs`. In addition, the `base` shared library contains the `TCMSJetableParticle` class. This class does not contain any information about the particle history but keeps a representation in $\eta \times \phi$ space which is optimal for jet-finding algorithms. This representation is illustrated in the structure of the class shown in Figure A-4. The `TCMSJet` class

which represents jets can also be found in the base shared library.

```
class TCMSJetableParticle : public TObject {

private:
   Double_t       fEta;
   Double_t       fPhi;
   Double_t       fET;
   Double_t       fPt;
   Int_t          fPID;    //particle id
   Int_t          fStatus; //status code (KS in TMCParticle)

public:
      .
      .
      .
}
```

Figure A-4: Stub for the class TCMSJetableParticle included in the shared library base. This class avoids the overhead of calculating η, ϕ and E_T in jet-finding algorithms by storing these variables and making them the principal particle representation. This class is only intended for temporary storage when the $(\eta \times \phi)$ representation is going to be used often.

The tree shared library contains other data structures to keep generation information and the tree-maker class TCMSAnalysisTree. The data members of these remaining data structures are shown in Figure A-5. The classes introduced so far constitute all the current data storage machinery of CMSROOT. While the TCMSJet and TCMSJetableParticle are currently used for temporary storage only, all the other data storage classes are used by the TCMSAnalysisTree to store data permanently in a TTree with the particular CMSTree layout. This layout is outlined in Figure A-6.

The creation of a CMSTree structure is abstracted through the tree-maker class, TCMSAnalysisTree. Because the creation of the CMSTree is currently tied to the generation of data, the TCMSAnalysisTree class constitutes the interface between data generation and data storage. However, for the sake of expandability, this class does not need to have any knowledge about the generators. It interacts with them exclusively through the virtual methods provided by the abstract class TCMSGen. All the generator options, specific to each generator, are then available through the TCMSGen*

```
class TCMSMCInfo : public TObject {

private:
   Double_t fImpact; //Impact parameter
   TString  fName;   //Name of the MC (coincides with the saved .root file)
   Int_t    fPart;   //Number of participants
   Int_t    fCols;   //Number of collisions

public:
     .
     .
     .
}
class TCMSEventInfo : public TObject {

private:
   Int_t    fRunNo;     //Run Number
   Int_t    fEventNo;   //Event Number
   TDatime  fDate;      //Date and time of the event

public:
     .
     .
     .
}
```

Figure A-5: Fields used for information storage in the `TCMSMCInfo` and `TCMSEventInfo` classes.

`TCMSAnalysisTree::GetGenerator()` method. A complete discussion of the generator classes is deferred to Section A.2.2. Currently, the code in the `TCMSAnalysisTree` class accounts for different generator purposes, such as whether signal or background are being generated only. In this sense, the class needs to know what generator is being used. This has been a convenient design choice for the current use of the framework where post-processing of data coming from the generator is almost completely absent. The necessity of adding triggering capabilities and other post-processing operations has, however, recently become apparent to users and developers of CMSROOT. The addition of an extra layer of abstraction between the generators and the `TTree` creation with the purpose of handling such post-processing actions is being

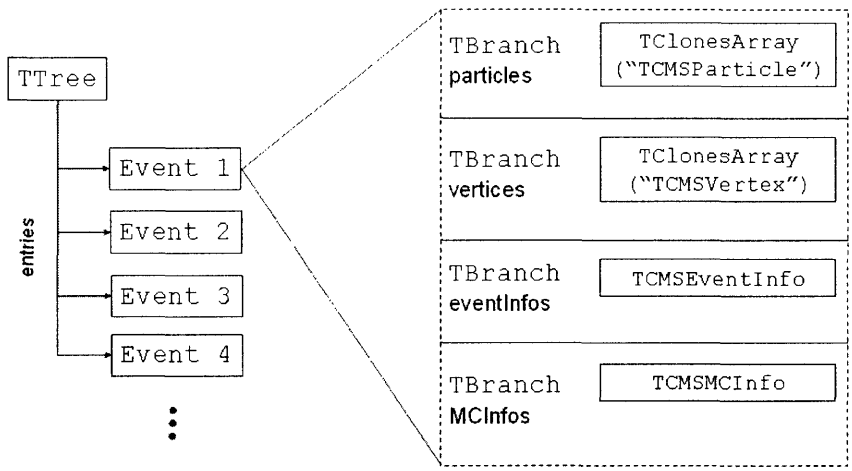

Figure A-6: Structure of a `CMSTree`. The four different `TBranches` and their names are shown.

considered. Finally, it is relevant to mention here we performed studies to determine the settings for the creation of a `TTree` in `CMSTree` format which optimize efficiency in storage. We found that a split level of 2 in the `TTree`[49] yields the best relation between creation time and occupied space. Therefore, all the `TTrees` created with `TCMSAnalysisTree` are split down to their second level.

This completes the main outline of the procedures by which generated data are stored. The classes in the `base` shared library are unlikely to change in the future, except for possible additions to represent physical entities that are required by different analyses. However, the classes in the `tree` shared library, having a more dynamic role, will evolve in the future to accommodate new functionality.

A.2.2 Interfaces to Monte Carlo generators

As mentioned in Section A.1, the Monte Carlo generators integrated into CMSROOT are all in the form of FORTRAN77 subroutines. In these subroutines, it is usual to make references and modify global variables called common-blocks, which maintain the state of the generator. This idea of a generator state justifies the definition of a C++ generator object whose state changes through methods which give access to the FORTRAN subroutines and common-blocks. The generators currently supported are

HYDRO[25, 31], PYTHIA[17] and PYQUEN[18, 30], represented by their homologous C++ classes: `TCMSHydro`, `TCMSPythia` and `TCMSPyquen`, respectively. Obviously, each of these generators have different common-blocks which require accessors which are specific to each generator. However, as mentioned in Section A.2.1 there is some functionality which is common to all generators. More specifically, all generators need to be able to:

- Generate an event.
- Access particles and vertices from the event that was generated.
- Log information about the settings used in the generation of the last event.

We abstracted this common required functionality under the `TCMSGen` abstract class. In particular, the first of these three functions is implemented through the purely virtual method `void TCMSGen::GenerateEvent()`. Particles and vertices are accessed simultaneously by reference to appropriately initialized `TClonesArrays` through the purely virtual method `ImportParticles(TClonesArray* particles, TClonesArray* vertices)` in `TCMSGen`. Finally, `TCMSGen::Log(FILE *fptr, Option_t* option)` abstracts the logging capability specified in the last point. In this way, all the functionality required by `TCMSAnalysisTree` is abstracted in `TCMSGen` and the former class needs no knowledge of what generators are currently available in the framework, as long as they adhere to the convention established by the base abstract class.

This convention is obviously respected by the currently available generators: `TCMSHydro`, `TCMSPythia` and `TCMSPyquen`. While both `TCMSHydro` and `TCMSPythia` are derived directly from `TCMSGen`, `TCMSPyquen` is a subclass of `TCMSPythia`. This is a very natural relation in light of the nature of PYQUEN as we introduced in Chapter 2. This class structure is illustrated in Figure A-7. It is important to note that, even though they implement the CMSROOT-specific methods defined in the abstract class, these generator classes are nothing more than C++ wrappers of their FORTRAN counterparts. As such, common-blocks or subroutines with the same name in two different generators are not distinguished. In the case of subroutines, this causes the first

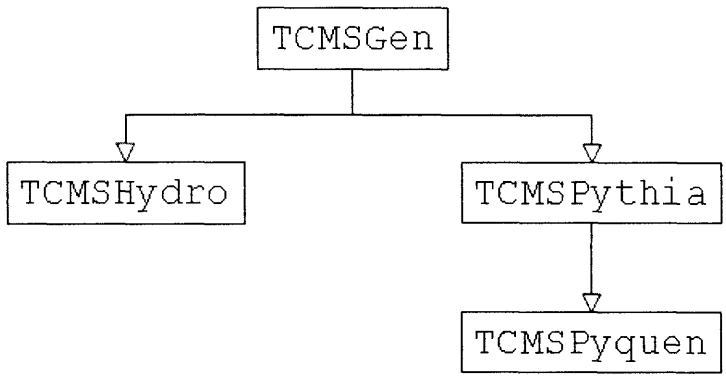

Figure A-7: Structure of the modules used for generating data in CMSROOT.

subroutine that was loaded, as part of a shared library, to be the one used exclusively, regardless of which shared library calls it. In the case of common-blocks, if the name of two common-blocks is repeated, then these common-blocks are shared through all shared libraries. This is not desired, because it can lead to confusion and undesired behavior, and has prevented us from adding the HIJING or HYDJET (HYDRO+PYTHIA/PYQUEN) generators to the current version of CMSROOT. Several solutions are being considered to solve this problem and extend the number of generators in our framework and a solution should be implemented shortly. In addition, in order to render these wrapper classes fully functional, all the subroutines, functions and common-blocks must be translated from FORTRAN to C++. Due to the large amount of common blocks available in PYTHIA, performing this task has not yet been possible in `TCMSPythia`. However, the more commonly used set of subroutines and common-blocks has been made available for CMSROOT users; and the list of accessible common blocks is being continuously expanded.

This summarizes the most important features and limitations of the interfaces between the Monte Carlo generators and the C++ data analysis framework we developed. The basic class structure is likely to grow in the future. However, the goals and the approach to such expansion are likely to remain the same.

A.2.3 Data processing

Data processing in CMSROOT takes full advantage of the capabilities of the ROOT class `TSelector`. Being a native ROOT class, `TSelector` provides the desired interaction with `TTrees` for data analysis and support for use with PROOF, and it is, therefore, the natural starting point for any data processing tool in CMSROOT. Obviously, being a generic class for access to `TTrees`, `TSelector` has no knowledge about the specific structure of a `CMSTree`. In order to hide this structure from users of CMSROOT, we created a base abstract class from which all CMSROOT analysis classes must inherit: `TCMSSelector`. This class implements the following `TSelector` `virtual` methods required for loading `TTrees`:

- `void TSelector::SlaveBegin(TTree* tree)`
- `void TSelector::Init(TTree* tree)`
- `Bool_t TSelector::Notify()`

The implementations of the `Begin()` (for histogram initialization), `Process()` (for analysis code) and `Terminate()` (for logging and saving actions) methods are left to each of the subclasses. Effectively, these three methods are the only ones that need to be implemented by users creating their own data analysis classes.

The original development of CMSROOT required the support of mixing signal and background events during the analysis. For this reason, `TCMSSelector` allows the user to load two `TTrees` simultaneously. The `Process()` method should be called on the background `TTree`, while, if desired, the signal `TTree` should be specified as input to the `TCMSSelector` through `SetOption(TList* list)`, where the `list` argument should contain a `TString*` with the filename where the signal tree is stored. Such an input guarantees that the background and signal `TTrees` are loaded into the `protected` `TCMSSelector` data members `fBackTree` and `fSignalTree`, respectively. Similarly, the specific `TBranches` are loaded into the data members `fSignalPartBranch`, `fSignalVertBranch`, `fBackPartBranch`, `fBackVertBranch`, `fEventBranch` and `fMCBranch`. The corresponding data members provided to store the leaves are: `fSignalParticles`,

`fSignalVertices`, `fBackParticles`, `fBackVertices`, `fEventInfo` and `fMCInfo`. Note, however, that this design responds to a very specific design requirement which may change as the development of CMSROOT continues. If different kind of analyses involving a variable number of `TTree`s are foreseen, the addition of new classes inheriting from `TSelector` or the generalization of the current `TCMSSelector` might be required.

In addition, `TCMSSelector` contains additional member fields for specifying acceptance cuts and the name of a log file. This name is used by different `protected` utility methods included in `TCMSSelector`. These methods use the extension-less filename provided through `TCMSSelector::SetOutputFile(TString* log)` for saving `TCanvas`es in different formats and creating a log file with the name of the files and the acceptance cuts used in the analysis.

Another base analysis class, which was especially important for the analyses presented in this thesis, is included in CMSROOT. This class, `TCMSJetAnalysis`, contains `protected` methods implementing jet finding algorithms. Therefore, all data analysis classes which need to perform jet analyses should inherit from this class. Several analysis classes created for the purpose of the analyses presented in this thesis are currently present in CMSROOT. The current list is too long and likely to change. However, some of them are shown in Figure A-8, where the class structure of our selector classes is illustrated.

A.3 Further Development and Conclusions

The previous sections provided an overview of the design considerations that went into the development of CMSROOT, and how these considerations translated into specific design choices. In addition, we have emphasized the design considerations which have changed or are likely to change as the range of applications of CMSROOT grows, and mentioned some of the solutions that are being considered in order to address these changes. Summarizing, CMSROOT is a general-purpose analysis framework within the CMS Heavy-Ion community and, as such, its possible areas of application are still

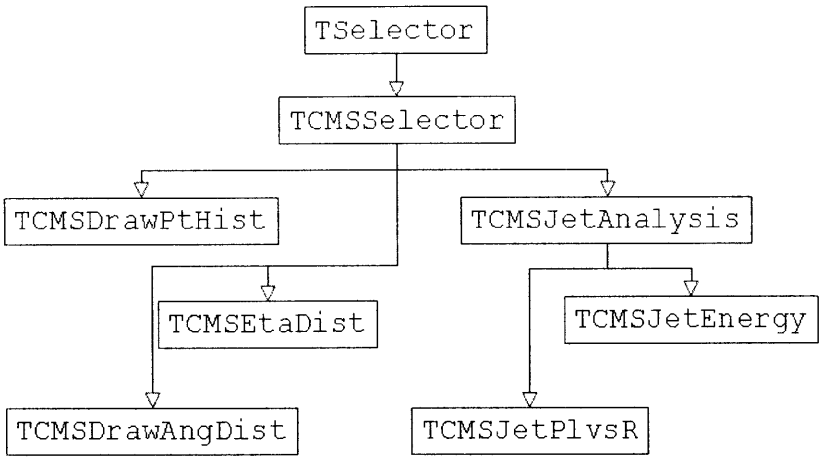

Figure A-8: Structure of data analysis classes in CMSROOT. Note all CMSROOT selectors inherit from `TCMSSelector`, which is itself a subclass of `TSelector`. In addition, all classes which require jet finding algorithms either at the Monte Carlo or the calorimeter level are derived from the `TCMSJetAnalysis` class.

being explored. As this exploration continues, the framework will continue to evolve. Here, we have provided the picture behind the original conception of CMSROOT. An example of the power of the framework thus far developed are the results presented this thesis, which would have been impossible to obtain without the development of CMSROOT.

Bibliography

[1] D. Gross and F. Wilczek. *Phys. Rev. D*, 8:3633, 1973

[2] J. Harris and B. Müller. "The Search for the Quark-Gluon Plasma", hep-ph/9602235, 1996

[3] F. Karsch, *Nucl. Phys. A*,698:199, 2002, hep-ph/0103314

[4] P. Jacobs and X-N. Wang. "Matter in extremis: ultrarelativistic nuclear collisions at RHIC", hep-ph/0405125, 2004

[5] M. Breidenbach *et al.*, *Phys. Rev. Lett.*, 23:935, 1969

[6] U. A. Wiedemann, "Theoretical Overview QM '04 ", hep-ph/0402251, 2004

[7] U. A. Wiedemann *et al.*, "Hard Probes in Heavy Ion Collisions at the LHC: Jet Physics", hep-ph/0310274, 2003

[8] J. F. Owens, *Rev. Mod. Phys.*,Vol. 59, No. 2, 465 1987

[9] G. Roland, "The Physics of Relativistic Heavy Ion Collisions", Conference Talk at the Nuclear Physics Summer School, 2004

[10] A. Casher *et al.*, *Phys. Rev. D*,10:732, 1974

[11] C. Adler *et al.* [STAR Collaboration], *Phys. Rev. Lett.*,90:082302, 2003. Also available at nucl-ex/0308020

[12] X.-N. Wang and M. Gyulassy, *Phys. Rev. Lett.*,86:3496, 2001. Also available at nucl-th/0008014

[13] J. A. Lopez *et al.*, *Phys. Rev. Lett.*, 53:1216, 1984

[14] K. J. Eskola, *Nucl.Phys.*, A698 (2002) 78-87. Also available at hep-ph/0104058

[15] V. Topor Pop *et al.*,*Phys.Rev. C* 68:054902, 2003. Also available at nucl-th/0209089

[16] U. W. Heinz and P. F. Kolb, hep-ph/0204061

[17] T. Sjöstrand, Comp. Phys. Com. 135 (2001) 238. Also available at: http://www.thep.lu.se/ torbjorn/Pythia.html

[18] I. P. Lokhtin and A. M. Snigirev, "Fast simulation of jet quenching in ultrarelativistic heavy ion collisions", hep-ph/0406038, 2004

[19] K. H. Ackermann *et al.* [STAR Collaboration], *Phys. Rev. Lett.*, 86:402, 2001

[20] J.-Y. Ollitrault, *Phys. Rev. D* 86:229, 1992

[21] A. M. Poskanzer and S. A. Voloshin, *Phys. Rev. C* 58:1671, 1998

[22] X.-N. Wang, M. Gyulassy, *Phys. Rev. D* 44:3501, 1991

[23] D. Teaney, J. Lauret and E. V. Shuryak, *Phys. Rev. Lett.* 86:4783, 2001

[24] C. Adler *et al.* [STAR Collaboration], *Phys. Rev. Lett.* 89:202301, 2002

[25] I. P. Lokhtin and A. M. Snigirev, "Fast simulation of flow effects in central and semi-central heavy ion collisions at LHC", hep-ph/0312204, 2003

[26] S. S. Adler *et al.* [PHENIX Collaboration], "Saturation of azimuthal anisotropy in Au + Au collisions at $\sqrt{s_{NN}}$ = 62 - 200 GeV", nucl-ex/0411040

[27] B. B. Back *et al.* [PHOBOS Collaboration], *Phys. Rev. Lett.* 87:102301, 2001

[28] B. B. Back *et al.* [PHOBOS Collaboration], *Phys. Lett. B* 578:297, 2004

[29] C. Loizides, "Jet Physics in ALICE", nucl-ex/0501017, 2005

[30] http://lokhtin.home.cern.ch/lokhtin/pyquen/ (version: May 2005)

[31] http://lokhtin.home.cern.ch/lokhtin/hydro/

[32] R. Baier, Yu. L. Dokshitzer, A. H. Mueller and D. Schiff, *Phys. Rev. C* 60:064902, 1999

[33] J. D. Bjorken, Fermilab publication Pub-82/29-THY, 1982

[34] S. Mrówczyński, *Phys. Lett. B* 269:383, 1991

[35] I. P. Lokhtin and A. M. Snigirev, *Phys. Ltt. B* 440:163, 1998

[36] W. Busza, *Acta Phys.Polon.B* 35: 2873-2894, 2004. Also available at nucl-ex/0410035

[37] K. J. Eskola, K. Kajantie and P. V. Ruuskanen, *Phys. Lett. B* 332:191, 1994. Also available at hep-ph/9404237

[38] J. Adams *et al.* [STAR Collaboration], *Phys. Rev. Lett.* 91:172302, 2003

[39] S. S. Adler *et al.* [PHENIX Collaboration], *Phys. Rev. C* 69:034910, 2004. Also available at nucl-ex/0308006

[40] B. B. Back *et al.* [PHOBOS Collaboration], "The PHOBOS perspective on discoveries at RHIC". Accepted for Publication in *Nucl. Phys A*

[41] A. Moraes, C. Buttar and I. Dawson, "Prediction for Minimum Bias and the Underlying Event at LHC Energies", ATL-COM-PHYS-2005-010 March 2005

[42] P. Shukla, "Glauber Model for Heavy-Ion Collisions from Low Energies to High Energies". Available at nucl-th/0112039

[43] G. C. Blazey *et al.*, "Run II Jet Physics". Available at hep-ex/0005012

[44] CMS Outreach: http://cmsinfo.cern.ch/Welcome.html/

[45] CMS HCAL Technical Design Report (CERN/LHCC 97-31, CMS TDR 2, 20 June 1997)

[46] CMS ECAL Technical Design Report (CERN/LHCC 97-33, CMS TDR 4, 15 December 1997)

[47] I. Vardanyan, O. Kodolova and A. Oulianov, "Jet reconstruction in Heavy Ion events with CMS calorimeter", CMS AN 2003-004, 2003.

[48] http://root.cern.ch/

[49] http://root.cern.ch/root/doc/RootDoc.html

[50] http://www-zeus.desy.de/ burow/cfortran/index.htm